CDF/PUB/EXOTIC/CDFR/****
PRD draft version 4.3

Search for Standard Model Higgs Boson Production in Association with a W Boson at CDF

T. Aaltonen,[21] B. Álvarez González[w],[9] S. Amerio,[41] D. Amidei,[32] A. Anastassov,[36] A. Annovi,[17] J. Antos,[12] G. Apollinari,[15] J.A. Appel,[15] A. Apresyan,[46] T. Arisawa,[56] A. Artikov,[13] J. Asaadi,[51] W. Ashmanskas,[15] B. Auerbach,[59] A. Aurisano,[51] F. Azfar,[40] W. Badgett,[15] A. Barbaro-Galtieri,[26] V.E. Barnes,[46] B.A. Barnett,[23] P. Barria[dd],[44] P. Bartos,[12] M. Bauce[bb],[41] G. Bauer,[30] F. Bedeschi,[44] D. Beecher,[28] S. Behari,[23] G. Bellettini[cc],[44] J. Bellinger,[58] D. Benjamin,[14] A. Beretvas,[15] A. Bhatti,[48] M. Binkley*,[15] D. Bisello[bb],[41] I. Bizjak[hh],[28] K.R. Bland,[5] B. Blumenfeld,[23] A. Bocci,[14] A. Bodek,[47] D. Bortoletto,[46] J. Boudreau,[45] A. Boveia,[11] L. Brigliadori[aa],[6] C. Bromberg,[33] E. Brucken,[21] M. Bucciantonio[cc],[44] J. Budagov,[13] H.S. Budd,[47] S. Budd,[22] K. Burkett,[15] G. Busetto[bb],[41] P. Bussey,[19] A. Buzatu,[31] A. Calamba,[10] C. Calancha,[29] S. Camarda,[4] M. Campanelli,[28] M. Campbell,[32] F. Canelli[11],[15] B. Carls,[22] D. Carlsmith,[58] R. Carosi,[44] S. Carrillo[k],[16] S. Carron,[15] B. Casal,[9] M. Casarsa,[60] A. Castro[aa],[6] P. Catastini,[20] D. Cauz,[60] V. Cavaliere,[22] M. Cavalli-Sforza,[4] A. Cerri[e],[26] L. Cerrito[q],[28] Y.C. Chen,[1] M. Chertok,[7] G. Chiarelli,[44] G. Chlachidze,[15] F. Chlebana,[15] K. Cho,[25] D. Chokheli,[13] J.P. Chou,[20] W.H. Chung,[58] Y.S. Chung,[47] C.I. Ciobanu,[42] M.A. Ciocci[dd],[44] A. Clark,[18] G. Compostella[bb],[41] M.E. Convery,[15] J. Conway,[7] M.Corbo,[42] M. Cordelli,[17] C.A. Cox,[7] D.J. Cox,[7] F. Crescioli[cc],[44] C. Cuenca Almenar,[59] J. Cuevas[w],[9] R. Culbertson,[15] D. Dagenhart,[15] N. d'Ascenzo[u],[42] M. Datta,[15] P. de Barbaro,[47] S. De Cecco,[49] M. Dell'Orso[cc],[44] L. Demortier,[48] M. Deninno,[6] F. Devoto,[21] M. d'Errico[bb],[41] A. Di Canto[cc],[44] B. Di Ruzza,[44] J.R. Dittmann,[5] M. D'Onofrio,[27] S. Donati[cc],[44] P. Dong,[15] M. Dorigo,[60] T. Dorigo,[41] K. Ebina,[56] A. Elagin,[51] A. Eppig,[32] R. Erbacher,[7] D. Errede,[22] S. Errede,[22] N. Ershaidat[z],[42] R. Eusebi,[51] H.C. Fang,[26] S. Farrington,[40] M. Feindt,[24] J.P. Fernandez,[29] C. Ferrazza[ee],[44] R. Field,[16] G. Flanagan[s],[46] R. Forrest,[7] M.J. Frank,[5] M. Franklin,[20] J.C. Freeman,[15] Y. Funakoshi,[56] I. Furic,[16] M. Gallinaro,[48] J.E. Garcia,[18] A.F. Garfinkel,[46] P. Garosi[dd],[44] H. Gerberich,[22] E. Gerchtein,[15] S. Giagu[ff],[49] V. Giakoumopoulou,[3] P. Giannetti,[44] K. Gibson,[45] C.M. Ginsburg,[15] N. Giokaris,[3]

* Deceased

P. Giromini,[17] M. Giunta,[44] G. Giurgiu,[23] V. Glagolev,[13] D. Glenzinski,[15] M. Gold,[35] D. Goldin,[51] N. Goldschmidt,[16] A. Golossanov,[15] G. Gomez,[9] G. Gomez-Ceballos,[30] M. Goncharov,[30] O. González,[29] I. Gorelov,[35] A.T. Goshaw,[14] K. Goulianos,[48] S. Grinstein,[4] C. Grosso-Pilcher,[11] R.C. Group[55],[15] J. Guimaraes da Costa,[20] Z. Gunay-Unalan,[33] C. Haber,[26] S.R. Hahn,[15] E. Halkiadakis,[50] A. Hamaguchi,[39] J.Y. Han,[47] F. Happacher,[17] K. Hara,[53] D. Hare,[50] M. Hare,[54] R.F. Harr,[57] K. Hatakeyama,[5] C. Hays,[40] M. Heck,[24] J. Heinrich,[43] M. Herndon,[58] S. Hewamanage,[5] A. Hocker,[15] W. Hopkins[f],[15] D. Horn,[24] S. Hou,[1] R.E. Hughes,[37] M. Hurwitz,[11] U. Husemann,[59] N. Hussain,[31] M. Hussein,[33] J. Huston,[33] G. Introzzi,[44] M. Iori[ff],[49] A. Ivanov[o],[7] E. James,[15] D. Jang,[10] B. Jayatilaka,[14] E.J. Jeon,[25] S. Jindariani,[15] W. Johnson,[7] M. Jones,[46] K.K. Joo,[25] S.Y. Jun,[10] T.R. Junk,[15] T. Kamon,[51] P.E. Karchin,[57] A. Kasmi,[5] Y. Kato[n],[39] W. Ketchum,[11] J. Keung,[43] V. Khotilovich,[51] B. Kilminster,[15] D.H. Kim,[25] H.S. Kim,[25] H.W. Kim,[25] J.E. Kim,[25] M.J. Kim,[17] S.B. Kim,[25] S.H. Kim,[53] Y.K. Kim,[11] N. Kimura,[56] M. Kirby,[15] K. Knoepfel,[15] K. Kondo*,[56] D.J. Kong,[25] J. Konigsberg,[16] A.V. Kotwal,[14] M. Kreps,[24] J. Kroll,[43] D. Krop,[11] M. Kruse,[14] V. Krutelyov[c],[51] T. Kuhr,[24] M. Kurata,[53] S. Kwang,[11] A.T. Laasanen,[46] S. Lami,[44] S. Lammel,[15] M. Lancaster,[28] R.L. Lander,[7] K. Lannon[v],[37] A. Lath,[50] G. Latino[cc],[44] T. LeCompte,[2] E. Lee,[51] H.S. Lee,[11] J.S. Lee,[25] S.W. Lee[x],[51] S. Leo[cc],[44] S. Leone,[44] J.D. Lewis,[15] A. Limosani[r],[14] C.-J. Lin,[26] J. Linacre,[40] M. Lindgren,[15] E. Lipeles,[43] A. Lister,[18] D.O. Litvintsev,[15] C. Liu,[45] H. Liu,[55] Q. Liu,[46] T. Liu,[15] S. Lockwitz,[59] A. Loginov,[59] D. Lucchesi[bb],[41] J. Lueck,[24] P. Lujan,[26] P. Lukens,[15] G. Lungu,[48] J. Lys,[26] R. Lysak,[12] R. Madrak,[15] K. Maeshima,[15] K. Makhoul,[30] S. Malik,[48] G. Manca[a],[27] A. Manousakis-Katsikakis,[3] F. Margaroli,[46] C. Marino,[24] M. Martínez,[4] R. Martínez-Ballarín,[29] P. Mastrandrea,[49] M.E. Mattson,[57] A. Mazzacane,[15] P. Mazzanti,[6] K.S. McFarland,[47] P. McIntyre,[51] R. McNulty[i],[27] A. Mehta,[27] P. Mehtala,[21] A. Menzione,[44] C. Mesropian,[48] T. Miao,[15] D. Mietlicki,[32] A. Mitra,[1] H. Miyake,[53] S. Moed,[15] N. Moggi,[6] M.N. Mondragon[k],[15] C.S. Moon,[25] R. Moore,[15] M.J. Morello,[44] J. Morlock,[24] P. Movilla Fernandez,[15] A. Mukherjee,[15] Th. Muller,[24] P. Murat,[15] M. Mussini[aa],[6] J. Nachtman[m],[15] Y. Nagai,[53] J. Naganoma,[56] I. Nakano,[38] A. Napier,[54] J. Nett,[51] C. Neu,[55] M.S. Neubauer,[22] J. Nielsen[d],[26] L. Nodulman,[2] O. Norniella,[22] E. Nurse,[28] L. Oakes,[40] S.H. Oh,[14] Y.D. Oh,[25] I. Oksuzian,[55] T. Okusawa,[39] R. Orava,[21]

L. Ortolan,[4] S. Pagan Griso[bb],[41] C. Pagliarone,[60] E. Palencia[e],[9] V. Papadimitriou,[15] A.A. Paramonov,[2] J. Patrick,[15] G. Pauletta[gg],[60] M. Paulini,[10] C. Paus,[30] D.E. Pellett,[7] A. Penzo,[60] T.J. Phillips,[14] G. Piacentino,[44] E. Pianori,[43] J. Pilot,[37] K. Pitts,[22] C. Plager,[8] L. Pondrom,[58] S. Poprocki[f],[15] K. Potamianos,[46] O. Poukhov*,[13] F. Prokoshin[y],[13] A. Pranko,[15] F. Ptohos[g],[17] G. Punzi[cc],[44] A. Rahaman,[45] V. Ramakrishnan,[58] N. Ranjan,[46] I. Redondo,[29] P. Renton,[40] M. Rescigno,[49] T. Riddick,[28] F. Rimondi[aa],[6] L. Ristori[44],[15] A. Robson,[19] T. Rodrigo,[9] T. Rodriguez,[43] E. Rogers,[22] S. Rolli[h],[54] R. Roser,[15] M. Rossi,[60] F. Rubbo,[15] F. Ruffini[dd],[44] A. Ruiz,[9] J. Russ,[10] V. Rusu,[15] A. Safonov,[51] W.K. Sakumoto,[47] Y. Sakurai,[56] L. Santi[gg],[60] L. Sartori,[44] K. Sato,[53] V. Saveliev[u],[42] A. Savoy-Navarro,[42] P. Schlabach,[15] A. Schmidt,[24] E.E. Schmidt,[15] M.P. Schmidt*,[59] M. Schmitt,[36] T. Schwarz,[7] L. Scodellaro,[9] A. Scribano[dd],[44] F. Scuri,[44] A. Sedov,[46] S. Seidel,[35] Y. Seiya,[39] A. Semenov,[13] F. Sforza[cc],[44] A. Sfyrla,[22] S.Z. Shalhout,[7] T. Shears,[27] P.F. Shepard,[45] M. Shimojima[t],[53] M. Shochet,[11] I. Shreyber,[34] A. Simonenko,[13] P. Sinervo,[31] A. Sissakian*,[13] J. Slaunwhite[v],[37] K. Sliwa,[54] J.R. Smith,[7] F.D. Snider,[15] A. Soha,[15] V. Sorin,[4] P. Squillacioti,[44] M. Stancari,[15] M. Stanitzki,[59] R. St. Denis,[19] B. Stelzer,[31] O. Stelzer-Chilton,[31] D. Stentz,[36] J. Strologas,[35] G.L. Strycker,[32] Y. Sudo,[53] A. Sukhanov,[15] I. Suslov,[13] A. Taffard[b],[22] K. Takemasa,[53] Y. Takeuchi,[53] J. Tang,[11] M. Tecchio,[32] P.K. Teng,[1] J. Thom[f],[15] J. Thome,[10] G.A. Thompson,[22] E. Thomson,[43] P. Ttito-Guzmán,[29] D. Toback,[51] S. Tokar,[12] K. Tollefson,[33] T. Tomura,[53] D. Tonelli,[15] S. Torre,[17] D. Torretta,[15] P. Totaro,[41] M. Trovato[ee],[44] Y. Tu,[43] F. Ukegawa,[53] S. Uozumi,[25] A. Varganov,[32] F. Vázquez[k],[16] G. Velev,[15] C. Vellidis,[15] M. Vidal,[29] I. Vila,[9] R. Vilar,[9] J. Vizán,[9] M. Vogel,[35] G. Volpi,[17] P. Wagner,[43] R.L. Wagner,[15] T. Wakisaka,[39] R. Wallny,[8] S.M. Wang,[1] A. Warburton,[31] D. Waters,[28] W.C. Wester III,[15] D. Whiteson[b],[43] A.B. Wicklund,[2] E. Wicklund,[15] S. Wilbur,[11] F. Wick,[24] H.H. Williams,[43] J.S. Wilson,[37] P. Wilson,[15] B.L. Winer,[37] P. Wittich[f],[15] S. Wolbers,[15] H. Wolfe,[37] T. Wright,[32] X. Wu,[18] Z. Wu,[5] K. Yamamoto,[39] T. Yang,[15] U.K. Yang[p],[11] Y.C. Yang,[25] W.-M. Yao,[26] G.P. Yeh,[15] K. Yi[m],[15] J. Yoh,[15] K. Yorita,[56] T. Yoshida[j],[39] G.B. Yu,[14] I. Yu,[25] S.S. Yu,[15] J.C. Yun,[15] A. Zanetti,[60] Y. Zeng,[14] and S. Zucchelli[aa6]

(CDF Collaboration[†])

(CDF Collaboration)

[1]*Institute of Physics, Academia Sinica,*
Taipei, Taiwan 11529, Republic of China
[2]*Argonne National Laboratory, Argonne, Illinois 60439, USA*
[3]*University of Athens, 157 71 Athens, Greece*
[4]*Institut de Fisica d'Altes Energies, ICREA,*
Universitat Autonoma de Barcelona,
E-08193, Bellaterra (Barcelona), Spain
[5]*Baylor University, Waco, Texas 76798, USA*
[6]*Istituto Nazionale di Fisica Nucleare Bologna,*
[aa]*University of Bologna, I-40127 Bologna, Italy*
[7]*University of California, Davis, Davis, California 95616, USA*
[8]*University of California, Los Angeles,*
Los Angeles, California 90024, USA
[9]*Instituto de Fisica de Cantabria, CSIC-University of Cantabria, 39005 Santander, Spain*
[10]*Carnegie Mellon University, Pittsburgh, Pennsylvania 15213, USA*
[11]*Enrico Fermi Institute, University of Chicago, Chicago, Illinois 60637, USA*
[12]*Comenius University, 842 48 Bratislava,*
Slovakia; Institute of Experimental Physics, 040 01 Kosice, Slovakia

[†] With visitors from [a]Istituto Nazionale di Fisica Nucleare, Sezione di Cagliari, 09042 Monserrato (Cagliari), Italy, [b]University of CA Irvine, Irvine, CA 92697, USA, [c]University of CA Santa Barbara, Santa Barbara, CA 93106, USA, [d]University of CA Santa Cruz, Santa Cruz, CA 95064, USA, [e]CERN,CH-1211 Geneva, Switzerland, [f]Cornell University, Ithaca, NY 14853, USA, [g]University of Cyprus, Nicosia CY-1678, Cyprus, [h]Office of Science, U.S. Department of Energy, Washington, DC 20585, USA, [i]University College Dublin, Dublin 4, Ireland, [j]University of Fukui, Fukui City, Fukui Prefecture, Japan 910-0017, [k]Universidad Iberoamericana, Mexico D.F., Mexico, [l]Iowa State University, Ames, IA 50011, USA, [m]University of Iowa, Iowa City, IA 52242, USA, [n]Kinki University, Higashi-Osaka City, Japan 577-8502, [o]Kansas State University, Manhattan, KS 66506, USA, [p]University of Manchester, Manchester M13 9PL, United Kingdom, [q]Queen Mary, University of London, London, E1 4NS, United Kingdom, [r]University of Melbourne, Victoria 3010, Australia, [s]Muons, Inc., Batavia, IL 60510, USA, [t]Nagasaki Institute of Applied Science, Nagasaki, Japan, [u]National Research Nuclear University, Moscow, Russia, [v]University of Notre Dame, Notre Dame, IN 46556, USA, [w]Universidad de Oviedo, E-33007 Oviedo, Spain, [x]Texas Tech University, Lubbock, TX 79609, USA, [y]Universidad Tecnica Federico Santa Maria, 110v Valparaiso, Chile, [z]Yarmouk University, Irbid 211-63, Jordan, [hh]On leave from J. Stefan Institute, Ljubljana, Slovenia,

[13]*Joint Institute for Nuclear Research, RU-141980 Dubna, Russia*
[14]*Duke University, Durham, North Carolina 27708, USA*
[15]*Fermi National Accelerator Laboratory, Batavia, Illinois 60510, USA*
[16]*University of Florida, Gainesville, Florida 32611, USA*
[17]*Laboratori Nazionali di Frascati, Istituto Nazionale di Fisica Nucleare, I-00044 Frascati, Italy*
[18]*University of Geneva, CH-1211 Geneva 4, Switzerland*
[19]*Glasgow University, Glasgow G12 8QQ, United Kingdom*
[20]*Harvard University, Cambridge, Massachusetts 02138, USA*
[21]*Division of High Energy Physics, Department of Physics, University of Helsinki and Helsinki Institute of Physics, FIN-00014, Helsinki, Finland*
[22]*University of Illinois, Urbana, Illinois 61801, USA*
[23]*The Johns Hopkins University, Baltimore, Maryland 21218, USA*
[24]*Institut für Experimentelle Kernphysik, Karlsruhe Institute of Technology, D-76131 Karlsruhe, Germany*
[25]*Center for High Energy Physics: Kyungpook National University, Daegu 702-701, Korea; Seoul National University, Seoul 151-742, Korea; Sungkyunkwan University, Suwon 440-746, Korea; Korea Institute of Science and Technology Information, Daejeon 305-806, Korea; Chonnam National University, Gwangju 500-757, Korea; Chonbuk National University, Jeonju 561-756, Korea*
[26]*Ernest Orlando Lawrence Berkeley National Laboratory, Berkeley, California 94720, USA*
[27]*University of Liverpool, Liverpool L69 7ZE, United Kingdom*
[28]*University College London, London WC1E 6BT, United Kingdom*
[29]*Centro de Investigaciones Energeticas Medioambientales y Tecnologicas, E-28040 Madrid, Spain*
[30]*Massachusetts Institute of Technology, Cambridge, Massachusetts 02139, USA*
[31]*Institute of Particle Physics: McGill University, Montréal, Québec, Canada H3A 2T8; Simon Fraser University, Burnaby, British Columbia, Canada V5A 1S6; University of Toronto, Toronto, Ontario, Canada M5S 1A7; and TRIUMF,*

Vancouver, British Columbia, Canada V6T 2A3
[32]*University of Michigan, Ann Arbor, Michigan 48109, USA*
[33]*Michigan State University, East Lansing, Michigan 48824, USA*
[34]*Institution for Theoretical and Experimental Physics, ITEP, Moscow 117259, Russia*
[35]*University of New Mexico, Albuquerque, New Mexico 87131, USA*
[36]*Northwestern University, Evanston, Illinois 60208, USA*
[37]*The Ohio State University, Columbus, Ohio 43210, USA*
[38]*Okayama University, Okayama 700-8530, Japan*
[39]*Osaka City University, Osaka 588, Japan*
[40]*University of Oxford, Oxford OX1 3RH, United Kingdom*
[41]*Istituto Nazionale di Fisica Nucleare, Sezione di Padova-Trento,*
[bb]*University of Padova, I-35131 Padova, Italy*
[42]*LPNHE, Universite Pierre et Marie*
Curie/IN2P3-CNRS, UMR7585, Paris, F-75252 France
[43]*University of Pennsylvania, Philadelphia, Pennsylvania 19104, USA*
[44]*Istituto Nazionale di Fisica Nucleare Pisa,* [cc]*University of Pisa,*
[dd]*University of Siena and* [ee]*Scuola Normale Superiore, I-56127 Pisa, Italy*
[45]*University of Pittsburgh, Pittsburgh, Pennsylvania 15260, USA*
[46]*Purdue University, West Lafayette, Indiana 47907, USA*
[47]*University of Rochester, Rochester, New York 14627, USA*
[48]*The Rockefeller University, New York, New York 10065, USA*
[49]*Istituto Nazionale di Fisica Nucleare, Sezione di Roma 1,*
[ff]*Sapienza Università di Roma, I-00185 Roma, Italy*
[50]*Rutgers University, Piscataway, New Jersey 08855, USA*
[51]*Texas A&M University, College Station, Texas 77843, USA*
[52]*Istituto Nazionale di Fisica Nucleare Trieste/Udine,*
I-34100 Trieste, [gg]*University of Udine, Udine, Italy*
[53]*University of Tsukuba, Tsukuba, Ibaraki 305, Japan*
[54]*Tufts University, Medford, Massachusetts 02155, USA*
[55]*University of Virginia, Charlottesville, Virginia 22906, USA*
[56]*Waseda University, Tokyo 169, Japan*
[57]*Wayne State University, Detroit, Michigan 48201, USA*

[58]*University of Wisconsin, Madison, Wisconsin 53706, USA*
[59]*Yale University, New Haven, Connecticut 06520, USA*
[60]*Istituto Nazionale di Fisica Nucleare Trieste/Udine, I-34100 Trieste,* [gg]*University of Udine, I-33100 Udine, Italy*

(Dated: February 22, 2012)

Abstract

We present a search for the standard model Higgs boson production in association with a W boson in proton-antiproton collisions ($p\bar{p} \to W^{\pm}H \to \ell\nu b\bar{b}$) at a center of mass energy of 1.96 TeV. The search employs data collected with the CDF II detector which correspond to an integrated luminosity of approximately 2.7 fb^{-1}. We recorded this data with two kinds of triggers. The first kind required high-p$_T$ charged leptons and the second required both missing transverse energy and jets. The search selects events consistent with a signature of a single lepton ($e^{\pm}/\mu^{\pm}$), missing transverse energy, and two jets. Jets corresponding to bottom quarks are identified with a secondary vertex tagging method and a jet probability tagging method. Kinematic information is fed in an artificial neural network to improve discrimination between signal and background. The search finds that both the observed number of events and the neural network output distributions are consistent with the standard model background expectations, and sets 95% confidence level upper limits on the production cross section times branching ratio. The limits are expressed as a ratio to the standard model production rate. The limits range from 3.6 (4.3 expected) to 61.1 (43.2 expected) for Higgs masses from 100 to 150 GeV/c^2, respectively.

PACS numbers: 13.85.Rm, 14.80.Bn

I. INTRODUCTION

Standard electroweak theory predicts the existence of a single fundamental scalar particle, the Higgs boson, which arises as a result of spontaneous electroweak symmetry breaking [1]. The Higgs boson is the only fundamental standard model particle which has not been experimentally observed. Direct searches at LEP2 and the Tevatron have yielded constraints on the Higgs boson mass. LEP2 data exclude a Higgs boson with $m_H < 114.4\,\mathrm{GeV}/c^2$ at 95% confidence level (C.L.). Recently, the Tevatron has excluded at 95% C.L. the mass range $154 < m_H < 175\,\mathrm{GeV}/c^2$ [2]. In addition, recent global fits to electroweak data yielded a one-sided 95% confidence level upper limit of 158 GeV/c^2 [3]. If the experimental lower limit of $114.4\,\mathrm{GeV}/c^2$ is included in the fit, then the upper limit raises to 185 GeV/c^2.

The Higgs boson branching ratios depend on the particle's mass. If the Higgs boson has a low mass ($m_H < 135\,\mathrm{GeV}/c^2$), it decays mostly to $b\bar{b}$ [4]. If the Higgs boson has a high mass ($m_H > 135\,\mathrm{GeV}/c^2$), then it preferentially decays to W^+W^-.

Higgs boson production in association with a W boson (WH) is the most sensitive low-mass search channel at the Tevatron. WH production is more sensitive than ZH production because it has a larger cross section. It is more sensitive than direct Higgs production $gg \to H \to b\bar{b}$ because it has a smaller QCD background.

Searches for $WH \to \ell\nu b\bar{b}$ at $\sqrt{s} = 1.96\,\mathrm{TeV}$ have been recently reported by CDF using 1.9 fb^{-1} [5], and D0 using 1 fb^{-1} [6] and 5.4 fb^{-1} [6]. The CDF analysis looked for WH production in charged-lepton-triggered events. It improved on prior results by employing a combination of different jet flavor identification algorithms [7]. Flavor identification algorithms distinguish between jets that are induced by light partons (u, d, s, g) and jets containing the debris of heavy quarks (b, c). The analysis also introduced multivariate techniques that use several kinematic variables to distinguish signal from background. The analysis set upper limits on the Higgs boson production rate, defined as the cross section times branching ratio $\sigma \cdot \mathcal{B}$ for mass hypotheses ranging from 110 to $150\,\mathrm{GeV}/c^2$. The rate was constrained to be less than 1.0 pb at 95% C.L. for $m_H = 110$ and less than 1.2 pb for $150\,\mathrm{GeV}/c^2$. This corresponds to a limit of 7.5 to 102 times the standard model cross section. More recently, CDF has produced a search with 2.7 fb^{-1} of data that combines both neural network and matrix element techniques [8]. The search we present here is an ingredient in the most recent combination.

The new search for $WH \rightarrow \ell\nu b\bar{b}$ reported here builds on the previous CDF result by adding more data and introducing new analysis techniques for identifying W candidate events that have been recorded using triggers involving missing transverse energy $\not\!\!E_T$ and jets. We use 2.7 fb^{-1} of data in our search, which is an increase of nearly 50% over the prior search. Our analysis uses both events recorded with a charged-lepton trigger and events recorded by a trigger that selects missing transverse energy $\not\!\!E_T$ and two jets. The missing transverse energy vector is the negative of the vector sum of calorimeter tower energy deposits in the event. It is corrected for the transverse momentum of any muons in the event. $\not\!\!E_T$ is the magnitude of the missing transverse energy vector. Missing transverse energy suggests that a neutrino from a W decay was present in an event. We identify W candidates in $\not\!\!E_T$ + jet events using looser charged-lepton identification requirements that recover muons that fell into gaps in the muon system. We show that including these events significantly increases the search sample and that these new events have a purity that is comparable to the samples using charged-lepton triggers samples.

We describe the analysis as follows: in Section II we describe the CDF II detector. We explain the event selection criteria in Sec. III, focusing especially on the identification of loose muons. In Sec. III D we discuss the b-tagging algorithms. We estimate contributions from the standard model (SM) backgrounds and show the results in Sec. IV. In Sec. V, we estimate our signal acceptance and systematic uncertainties. Sec. VI describes the multivariate technique that we use to enhance our discrimination of signal from backgrounds. We report our measured limits in Sec. VII and interpret the result in Sec. VIII.

II. CDF II DETECTOR

The CDF II detector [9] geometry is described using a cylindrical coordinate system. The z-axis follows the proton direction, the azimuthal angle is ϕ, and the polar angle θ is usually expressed through the pseudorapidity $\eta = -\ln(\tan(\theta/2))$. The detector is approximately symmetric in η and about the z axis. The transverse energy is defined as $E_T = E \sin\theta$ and transverse momentum as $p_T = p \sin\theta$.

Charged particles are tracked by a system of silicon microstrip detectors and a large open cell drift chamber in the region $|\eta| \leq 2.0$ and $|\eta| \leq 1.0$, respectively. The open cell drift chamber is called the central outer tracker (COT). The tracking detectors are immersed

in a 1.4 T solenoidal magnetic field aligned coaxially with the incoming beams, allowing measurement of charged particle momentum.

The transverse momentum resolution is measured to be $\delta p_T/p_T \approx 0.1\% \cdot p_T(\mathrm{GeV})$ for the combined tracking system. The track impact parameter d_0 is the distance from the event vertex to the track's closest approach in the transverse plane. It has a resolution of $\sigma(d_0) \approx 40\,\mu$m of which 30 μm is due to the size of the beam spot.

Outside of the tracking systems and the solenoid, segmented calorimeters with projective tower geometry are used to reconstruct electromagnetic and hadronic showers [10–12] over the pseudorapidity range $|\eta| < 3.6$. A transverse energy is measured in each calorimeter tower where θ is calculated using the measured z position of the event vertex and the tower location.

Small contiguous groups of calorimeter towers with energy deposits are identified and summed together into an energy cluster. Jets are identified by summing energies deposited in electromagnetic (EM) and hadronic calorimeter (HAD) towers that fall within a cone of radius $\Delta R = \sqrt{(\Delta\phi^2 + \Delta\eta^2)} \leq 0.4$ units around a high-E_T seed cluster [13]. Jet energies are corrected for calorimeter non-linearity, losses in the gaps between towers and multiple primary interactions [14]. Electron candidates are identified in the central electromagnetic calorimeter (CEM) as isolated, electromagnetic clusters that match a track in the pseudorapidity range $|\eta| < 1.1$. The electron transverse energy is reconstructed from the electromagnetic cluster with a precision $\sigma(E_T)/E_T = 13.5\%/\sqrt{E_T/(\mathrm{GeV})} \oplus 2\%$ [10].

This analysis uses three separate muon detectors and the gaps in between the detectors to identify muon candidates. After at least five hadronic interaction lengths in the calorimeter, the muons encounter the first set of four layers of planar drift chambers (CMU). After passing through another 60 cm of steel, the muons reach an additional four layers of planar drift chambers (CMP). Muons require $p_T > 1.4\,\mathrm{GeV}/c$ to reach the CMU [15] and an $p_T > 2.0$ GeV/c to reach the CMP [16]. Muon candidates are then identified as tracks that extrapolate to line segments or "stubs" in one of the muon detectors. A track that is linked to both CMU and CMP stubs is called a CMUP muon. These two systems cover the same central pseudorapidity region with $|\eta| \leq 0.6$. Muons that exit the calorimeters at $0.6 \leq |\eta| \leq 1.0$ are detected by the CMX system of four drift layers and are called CMX muons. Tracks that point to a gap in the CMX or CMUP muon system are called isolated track muon candidates.

The CDF trigger system is a three-level filter, with tracking information available even at the first level [17]. Events used in this analysis have passed either the electron trigger, the muon trigger, or the missing transverse energy $\not\!\!E_T$ trigger selection. The lepton trigger selection is identical to the selection used in [5]. The first stage of the central electron trigger requires a track with $p_T > 8$ GeV/c pointing to a tower with $E_T > 8$ GeV and $E_{\rm HAD}/E_{\rm EM} < 0.125$, where $E_{\rm HAD}$ is the hadronic calorimeter energy and $E_{\rm EM}$ is the electromagnetic calorimeter energy. The first stage of the muon trigger requires a track with $p_T > 4$ GeV/c (CMUP) or 8 GeV/c (CMX) pointing to a muon stub. For lepton triggers, a complete lepton reconstruction is performed online in the final trigger stage, where we require $E_T > 18$ GeV/c^2 for central electrons (CEM), and $p_T > 18\,$GeV/c for muons (CMUP,CMX).

The $\not\!\!E_T$ plus two jets trigger has been previously used in the $V(=W,Z)H \rightarrow \not\!\!E_T + b\bar{b}$ Higgs search [18] and offers a chance to reconstruct WH events that did not fire the high-p_T lepton trigger. The trigger's requirements are two jets and missing transverse energy. The two jets must have $E_T > 10$ GeV, and one must be in the central region $|\eta| < 0.9$. The missing transverse energy calculation that is used in the trigger, $\not\!\!E_T^{\rm raw}$, assumes that primary vertex of the event is at the center of the detector and does not correct for muons. The trigger requires $\not\!\!E_T^{\rm raw} > 35$ GeV. Sections III and V discuss the implications of these trigger requirements on the event selection and trigger efficiency.

III. EVENT SELECTION

The observable final state from WH production and decay consists of a high-p_T lepton, missing transverse energy, and two jets. This section provides an overview of how we reconstruct and identify each part of the WH decay, focusing especially on isolated track reconstruction, which is new for this result. Additional details on the event reconstruction can be found in Ref. [5].

A. Lepton Identification

We use several different lepton identification algorithms in order to include events from multiple trigger paths. Each algorithm requires a single high-p_T (> 20 GeV/c), isolated

charged lepton consistent with leptonic W boson decay. We employ the same electron and muon identification algorithms as the CDF W cross section measurement [19] and the prior CDF WH search [5]. We classify the leptons according to the sub-detector that recorded them: CEM electrons, CMUP muons, and CMX muons. We supplement the lepton identification with an additional category called "isolated tracks". An isolated track event is required to have a single, energetic track that is isolated from other track activity in the event and that has not been reconstructed as an electron or a muon using the other algorithms mentioned above.

The isolated track selection is designed to complement the trigger muon selection in that it finds muons that did not leave hits in the muon chambers, and therefore, could not have fired the muon trigger. Figure 1 shows how isolated track events increase overall muon coverage. The isolated track events are concentrated in the regions where there is no other muon coverage. Including isolated track events increases the acceptance by 25% relative to the acceptance of charged-lepton triggers.

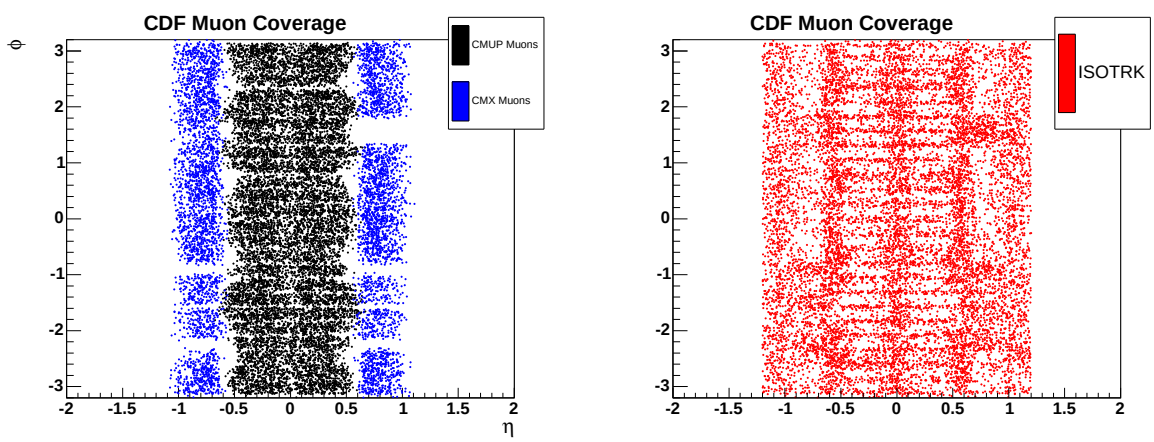

FIG. 1: (Left) Angular distribution of WH Monte Carlo muon triggered events. Note the cracks between CMUP chambers and the gap between the CMUP and CMX. (Right) Isolated track events recover high-p_T muons that fall in the muon chamber gaps.

We identify isolated tracks based on criteria used in the top lepton plus track cross section measurement [20]. Table I outlines the specific isolated track selection criteria. The track isolation variable quantifies the amount of track activity near the lepton candidate. It is

Variable	Cut
p_T	> 20 GeV/c
$\|z_0\|$	< 60 cm
$\|d_0\|$	< 0.02 cm
$\|d_0\|$ (no Si hits)	< 0.2 cm
track isolation	> 0.9
Axial COT hits	≥ 24
Stereo COT Hits	≥ 20
Num Si Hits (only if num expected hits ≥ 3)	≥ 3

TABLE I: Isolated track identification requirements. In the table, d_0 is the track impact parameter, d_0 (no Si Hits) is the impact parameter for tracks that have no silicon tracker hits, z_0 is position along the direction of the beamline of the closest approach of the track to the beamline, and the Axial and Stereo hits are on tracks the open cell drift chamber (COT). We define track isolation according to equation 1.

defined as

$$\text{TrkIsol} = \frac{p_T(candidate)}{p_T(candidate) + \sum p_T(trk)} \quad , \tag{1}$$

where $\sum p_T(trk)$ is the sum of the p_T of tracks that meet the requirements in Table II. Using this definition, a track with no surrounding activity has an isolation of 1.0. We require track isolation to be > 0.9.

We veto events with an identified charged lepton that fires the trigger (CEM, CMUP, CMX) in order to ensure that the data sets are disjoint. In addition, we veto events with two or more isolated tracks or a single isolated track that falls inside the cone of a jet ($\Delta R < 0.4$), as these events are unlikely to have come from $W \to \mu\nu$ decay.

B. Jet Selection

WH signal events have two high-E_T jets from the $H \to b\bar{b}$ decays. We define reconstructed jets using a cone of $\Delta R < 0.4$, where $\Delta R = \sqrt{\Delta\phi^2 + \Delta\eta^2}$. We require jets to have $E_T > 20$ GeV and $|\eta| < 2.0$. The η cut ensures that the jets are within the fiducial volume

Variable	Cut
p_T	> 0.5 GeV/c
ΔR(trk, candidate)	< 0.4
ΔZ(trk, candidate)	< 5 cm
Number of COT axial hits	> 20
Number of COT stereo hits	> 10

TABLE II: Requirements for tracks included in track isolation calculation.

Trigger Sample	Jet Selection
Charged Leptons	$E_T > 20$ GeV
	$\lvert\eta\rvert < 2.0$
$\not\!\!E_T$ + Jets	$E_T > 25$ GeV
	$\lvert\eta\rvert < 2.0$
	At least one jet $\lvert\eta\rvert < 0.9$
	$\Delta R > 1.0$

TABLE III: Jet selection criteria for events in our different trigger samples.

of the silicon detector. The jet energies are corrected to account for variations in calorimeter response in η, calorimeter non-linearity, and energy from additional interactions in the same bunch crossing. Monte Carlo simulations (MC) show that about 60% of WH events passing our selections result in two-jet events. The remainder is split evenly between events with one or three jets. Events with one or three jets have a worse signal-to-background ratio than those with two jets due to contamination from background processes such as W+jets and $t\bar{t}$, respectively. We limit our search for $WH \rightarrow \ell\nu b\bar{b}$ to events with W + exactly two jets.

For events collected on the $\not\!\!E_T$ + jets trigger, we require the jets to have an $E_T > 25$ GeV to ensure that they are above the trigger threshold. One of the two jets must be in the central region $|\eta| < 0.9$ to match the requirements of the trigger. In addition, because the trigger has a low efficiency for jets that are close together, we require the jets to be well-separated ($\Delta R > 1.0$).

Table III summarizes the jet selection criteria for events in each trigger sample.

In calculating event kinematics we find it useful to consider loose jets that have either somewhat smaller E_T than our cuts or have high-E_T but are further forward than our standard jets. We call these jets "loose jets". We do not use them directly in our event selection, but we do use them in calculating kinematic variables. We define loose jets to be jets with $E_T > 12$ GeV in the region $|\eta| < 2.0$, and $E_T > 20$ GeV in the region $2.0 < |\eta| < 2.4$.

C. Missing Transverse Energy

The presence of a neutrino from the W decay is inferred from the presence of a significant amount of missing transverse energy. The missing transverse energy vector is the negative of the vector sum of all calorimeter tower energy deposits with $|\eta| < 3.6$. The $\not\!\!E_T$ is the magnitude of the missing E_T vector. We correct the energy of jets in the event [14] and propagate the corrections to the $\not\!\!E_T$. We also account for the momentum of any high p_T muons. When we calculate $\not\!\!E_T$, we use z-position of the primary vertex to get the correct E_T for each calorimeter tower. Some events have more than one vertex. In this case, We use the sum of the transverse momentum of the tracks associated with each vertex to distinguish between the vertexes. The primary vertex is the one with the highest sum of the track transverse momentum. We then require $\not\!\!E_T$ to exceed 20 GeV.

D. b-jet identification

Both of the jets in WH events originate from $H \to b\bar{b}$ decays. Many backgrounds have jets that come from light-flavor partons (u, d, c, s, g), such as W + jets and QCD. Jets from b quarks can be distinguished from light-flavor jets by looking for the decay of long-lived B hadrons. We use the same b-jet identification strategy as the previous WH search [5]. We employ two separate algorithms to identify B hadrons. The secondary vertex tagging algorithm [21] takes tracks within a jet and attempts to reconstruct a secondary vertex. If a vertex is found and it is significantly displaced from the primary vertex, the jet is identified, or tagged, as a b jet. The Jet Probability algorithm [22] also uses tracking information inside of jets to identify B decays. Instead of requiring a secondary vertex, the algorithm looks at the distribution of impact parameters for tracks inside a jet. If the jet has a significant

number of large impact parameter tracks, then it is tagged as a b-jet. Jet probability tags have a lower purity than secondary vertex tags.

E. Lepton + Jets Selection

After identifying the final state objects in the event, we purify the sample with quality cuts. We fit a subset of well-measured tracks coming from the beamline to determine the event's primary vertex. The longitudinal coordinate z_0 of the lepton track's point of closest approach to the beamline must be within 5 cm of the primary vertex to ensure that the lepton and the jets come from the same hard interaction. We reduce backgrounds from Z boson decays by vetoing events where the invariant mass of the lepton and a second track with $p_T > 10\,\mathrm{GeV}/c$ falls in the Z-boson mass window $76 < m_{\ell-trk} < 106\,\mathrm{GeV}/c^2$.

We use the b-jet tagging strategy developed in the previous WH search [5]. We require at least one jet to be b-tagged with the secondary vertex algorithm, and then we divide our sample into three exclusive categories of varying purity. Events with two secondary vertex tagged jets have the highest purity, followed by events with one secondary vertex tagged jet and one jet probability tagged jet. In the lowest purity events, there is only one secondary vertex tagged jet.

We further purify the sample with exactly one secondary vertex tagged jet by using kinematic and angular cuts designed to reject QCD events with fake W signatures. The kinematics of the QCD contamination vary with the lepton signature they mimic. We therefore apply a separate veto to each lepton subsample.

One approach we use to reduce QCD is to cut on a variable correlated with mismeasurement. The observation of single top quark production [23] demonstrated that missing transverse energy significance $S_{\not\!\!E_T}$ is a useful variable to remove QCD contamination. Missing transverse energy significance $S_{\not\!\!E_T}$ quantifies the likelihood that the measured $\not\!\!E_T$ comes from jet mismeasurements. $S_{\not\!\!E_T}$ is defined as follows:

$$S_{\not\!\!E_T} = \frac{\not\!\!E_T}{(\sum_{jets} C_{JES}^2 \cos^2(\Delta\phi_{\not\!\!E_T,jet}) E_{T,jet}^{raw} + \cos^2(\Delta\phi_{\not\!\!E_T,uncl}) E_{T,uncl})^{1/2}} \ , \tag{2}$$

where C_{JES} is the jet energy correction factor, $\Delta\phi_{\not\!\!E_T,jet}$ is the azimuthal angle between the jet and the $\not\!\!E_T$ direction, $E_{T,jet}^{raw}$ is the uncorrected jet E_T, unclustered energy is energy not associated with a jet, $E_{T,uncl}$ is the transverse unclustered energy, and $\Delta\phi_{\not\!\!E_T,uncl}$ is the

Quantity	Cut
CEM	
M_T	> 20 GeV
$S_{\not{E}_T}$	$\geq -0.05 \cdot M_T + 3.5$
$S_{\not{E}_T}$	$\geq 2.5 - 3.125 \cdot \Delta\phi_{MET,jet2}$
CMUP,CMX	
M_T	> 10 GeV
ISOTRK	
M_T	> 10 GeV

TABLE IV: QCD veto cuts for each lepton category. These cuts are applied to events with exactly one identified b-jet.

azimuthal angle between the unclustered energy direction and the $\not{E}_T$ direction. The lower the value of $S_{\not{E}_T}$, the more likely it is that the $\not{E}_T$ comes from fluctuations in jet energy measurements. The uncertainty on the calorimeter energy not clustered into one of the jets is also included.

Another useful approach for rejecting QCD backgrounds is to require that the lepton momentum and $\not{E}_T$ be consistent with the decay of a W boson. However, since only the transverse component of the neutrino momentum is available via $\not{E}_T$, the W invariant mass cannot be calculated. Instead, if we ignore the neutrino p_z, we can calculate the transverse mass as follows:

$$M_T = \sqrt{2(p_T^{lep}\not{E}_T - \boldsymbol{p}_T{}^{lep} \cdot \boldsymbol{\not{E}}_T)} \tag{3}$$

We use both M_T and $S_{\not{E}_T}$ to remove QCD events from our sample. Table IV lists the different QCD veto cuts for each lepton type. The cuts were chosen to have high efficiency for events with a W boson while rejecting the maximum amount of QCD and minimizing disagreement between data and MC in the pretag sample.

IV. BACKGROUNDS

The signature of WH associated production is shared by a number of processes that can produce the combination $\ell\nu b\bar{b}$. The dominant backgrounds are W+jets production, $t\bar{t}$ production, single top production, and QCD multijet production. Diboson production and Z+jets production, collectively referred to as "electroweak backgrounds," contribute to the sample at smaller rates than any of the other backgrounds. Diboson production has a small contribution because of its small cross section and, in the case of WW, lack of b-jets at leading order. Z+jets production has a small contribution because it has a small overlap with our single lepton final state. Our estimate of the background rates uses a combination of Monte Carlo techniques and data-driven estimates. Our data-driven estimates use background-enriched control regions outside of our search region to determine background properties. We extrapolate the background properties from the control regions to the search region and assess an uncertainty on the estimates. Our background techniques are common to top cross section measurements [21], single top searches [24], and prior WH searches [25]. We provide an overview of the background estimate below and discuss the details of each background in the subsections that follow.

We first describe our background estimate for the sample of $\ell\nu jj$ events without any tagging requirements applied, which we refer to as the pretag sample. This sample is composed of events from two classes of processes: (1) events containing a high-p_T lepton from a real W decay and (2) events in which the lepton is from a source other than a W. In the second class of events, referred to as QCD multijet events, the high-p_T lepton comes either from a jet that fakes a lepton signature or from a real lepton produced in a heavy-flavor decay. After the QCD multijet background is subtracted off, what remains are events from a collection of processes that include the production of a W boson: primarily W + jets production, top production, and other electroweak backgrounds. We use a Monte Carlo based technique to estimate the relative contributions of processes whose rates and topologies are described well by next-to-leading order (NLO) calculations. These processes include $t\bar{t}$, single top and diboson, and Z + jets production. We estimate their expected contribution N using the theoretical NLO cross section σ, Monte Carlo event detection efficiency corrected to match the efficiency in the data ϵ, and the integrated luminosity of our dataset $\mathcal{L}_{int}$:

$$N = \sigma \cdot \epsilon \cdot \mathcal{L}_{int} \tag{4}$$

We subtract the contribution of these processes from the total number of observed events. After accounting both for the fraction of QCD multijet events and for the top and other electroweak processes, what remains are the pretag W+jets events, whose contribution is estimated as follows:

$$N_{W+Jets}^{Pretag} = N_{Pretag} \cdot (1 - F_{QCD}) - N_{EWK} - N_{TOP} \tag{5}$$

where N_{Pretag} is the observed number of $\ell\nu jj$ pretag events, N_{EWK} is the number of estimated electroweak events, and N_{TOP} is the number of estimated top events.

We estimate the number of tagged W + jets events using the number of pretag W + jet events and a tag probability. We measure the tag probabilities for both light and heavy-flavor jets in inclusive jet data. The tag probability for heavy-flavor jets is ϵ_{tag}, and the tag probability for falsely tagged jets, called "mistags", is ϵ_{mistag}. $W + b\bar{b}$, $W + c\bar{c}$, and $W + cq$ production are collectively referred to as W + heavy-flavor processes. All other W + jets production is referred to as W + light flavor. We use a b-tag scale factor to correct the Monte Carlo tagging efficiency according to the tag efficiency observed in data. We must estimate the fraction of W + jet events that are W + heavy-flavor events F_{HF} in our sample in order to use the appropriate tag probabilities. We use W + 1 jet data to calibrate the heavy-flavor fraction from the Monte Carlo. We use the ratio of the heavy-flavor fraction in the data F_{HF}^{data} to the heavy-flavor fraction in the Monte Carlo F_{HF}^{MC} to calculate a correction factor $K = F_{HF}^{data}/F_{HF}^{MC}$. We apply the correction factor to the number of W + heavy jets estimated with the Monte Carlo. After including this calibration, the number of W+jets in the tagged sample is:

$$N_{W+HF}^{tagged} = N_{W+jets}^{pretag} \cdot (F_{HF} \cdot K) \cdot \epsilon_{tag} \tag{6}$$

$$N_{W+LF}^{tagged} = N_{W+jets}^{pretag} \cdot (1 - F_{HF} \cdot K) \cdot \epsilon_{mistag} \tag{7}$$

The estimation of the rate of these backgrounds are done separately for each jet bin in the data. Below we describe the estimation of the individual pieces in greater detail.

Process	Theoretical Cross Section
WW	12.40 ± 0.80 pb
WZ	3.96 ± 0.06 pb
ZZ	1.58 ± 0.05 pb
Single top s-channel	0.88 ± 0.11 pb
Single top t-channel	1.98 ± 0.25 pb
$t\bar{t}$	6.7 ± 0.83 pb
Z + Jets	787.4 ± 85 pb

TABLE V: Theoretical cross sections [19, 26–28] and uncertainties for the electroweak and top backgrounds. Top cross sections assume a mass of $m_t = 175\,\mathrm{GeV}/c^2$.

A. Top and Electroweak Backgrounds

The normalization of the diboson, Z+jets, top-pair, and single-top backgrounds are based on the theoretical cross sections [19, 26–28] listed in Table V. The estimate from theory is well-motivated because the cross sections for most of the processes have small theoretical uncertainties. Z+jets is the only process where the large corrections to the leading order process give large uncertainties to the theoretical cross section. The impact of the large uncertainty on our sensitivity is marginalized by the small overlap of Z+jets with the W+jets final state. The background contributions are estimated using the theory cross sections, luminosity, and the Monte Carlo acceptance and b-tagging efficiency. The Monte Carlo acceptance is corrected for lepton identification, trigger efficiencies, and the z vertex cut. We also use a b-tagging scale factor to correct for the difference in tagging efficiency in Monte Carlo compared to data.

B. QCD Multijet

QCD multijet events can fake a W signature when a jet fakes a lepton and overall mismeasurement leads to fake $\not\!\!E_T$. Since these events do not have real W bosons in them, we also use the term non-W to refer to QCD multijet events. It is difficult to identify the precise sources of mismeasurement and handle them appropriately in a detector simulation. The

difficulty is increased by the large number of processes that contribute to the composition of the QCD background at unknown relative rates. Each lepton category is susceptible to different kinds of fakes. We use different QCD models for central-lepton triggered events and isolated track events.

We model central-lepton triggered QCD events using events where a jet fired the electron trigger, passed the electron kinematic cuts, but failed exactly two of the calorimeter or tracking quality cuts. Events that fail these cuts will have the kinematic properties of W events, including isolation, but the sample will be enriched in fakes. This is the same model used in the CDF observation of single top [23]. As noted in that paper, these fake events have the remarkable property that they model both electron and muon fakes.

We model QCD events that fake an isolated track by using events recorded on the $\not\!\!E_T$ + 2 Jets trigger. We use events with muon candidates that are not calorimeter isolated and are within the isolated track acceptance ($|\eta| < 1.2$). Calorimeter isolation is defined as the fraction of the lepton energy in a cone of $\Delta R = 0.4$ surrounding the lepton. Non-isolated leptons are unlikely to come from the decay of an on-shell W, and thus are enriched in fakes.

We estimate the amount of QCD background in each sample by fitting the $\not\!\!E_T$ spectrum in data. The fit includes the control region $\not\!\!E_T < 20$ GeV, which is enriched in QCD fakes. Figure 2 shows the $\not\!\!E_T$ fit for isolated track pretag events. The fit has one component with fixed normalization and two templates whose normalizations can vary. The fixed component is a combination of top and electroweak processes whose normalizations are described in Section IV A. We let the W + jets template vary along with the QCD template because there is a large uncertainty on the W+jets cross section. The QCD template has a $\not\!\!E_T$ spectrum that peaks near low $\not\!\!E_T$, and its normalization is driven by the low $\not\!\!E_T$ bins. The normalization of the W+jets template is driven by the high $\not\!\!E_T$ region. The fit determines the relative amounts of QCD and W+jets in the full $\not\!\!E_T$ sample, and we use these fit results to determine the QCD fraction in the search region ($\not\!\!E_T > 20$ GeV). For isolated track events with two jets and no b-tag requirement, we estimate a 19% QCD fraction in the signal region, as shown in Fig. 2. The pretag QCD fractions for the other lepton types are less than the isolated track fractions. Pretag CEM electrons events have 10% QCD fraction, and both CMUP and CMX muon events have a 3% QCD fraction. While isolated tracks have a larger amount of QCD events than the other lepton types, the vast majority of the isolated track events (81%) still contain W bosons. We use the QCD fractions for each lepton type and

tag category in the calculations for the background summaries in Tables VIII through XIII.

We estimate the uncertainty of the QCD normalization by studying the change in the QCD fraction due to changes in the QCD model. For tight lepton events we use an alternate QCD model based on leptons that fail our isolation requirements. We find a 40% uncertainty to the QCD normalization that covers the effect of using this alternative model. We use the same uncertainty estimate for both tight leptons and isolated tracks.

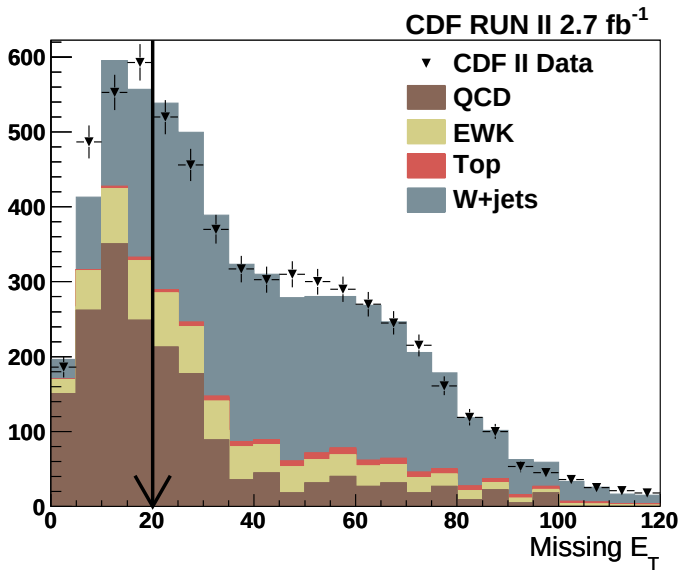

FIG. 2: Fit of the pretag isolated track $\not\!\!E_T$ control region that is used to determine the QCD fraction of isolated track events. The arrow illustrates the $\not\!\!E_T$ cut. We estimate a QCD fraction of 19% for the region with $\not\!\!E_T > 20$ GeV. There is some disagreement between the data and our model in the low-$\not\!\!E_T$ control region, and also around 50-55 GeV. The figure shows just one QCD model. The difference between this nominal model and are alternate covers the modelling difference shown here. We use the difference between the two models as our systematic uncertainty.

C. W+Heavy-Flavor

The number of W + heavy flavor events is a fraction the number of W + light flavor events, as described by F_{HF} in Equations 6 and 7. The fraction of W+heavy-flavor events has been studied extensively and is modeled in the ALPGEN Monte Carlo Generator [29, 30]. We calibrate the ALPGEN Version 2 W + jets Monte Carlo heavy-flavor fraction to match the

observed heavy flavor fraction in the $W + 1$ jet control region. We use the same calibration of the heavy-flavor fraction as the single top observation [23]. The calibration uses template fits of flavor-separating variables in b-tagged $W + 1$ jet data to measure the heavy flavor fraction. The calibration measures K, the calibration factor as defined in equation 6, to be $K = 1.4 \pm 0.4$.

We can estimate the amount of W + heavy flavor events in our signal region by calculating the efficiency for these events to pass our tag requirements ϵ_{tag}. The efficiency ϵ_{tag} is

$$\epsilon_{tag} = 1 - \prod_{i}^{jets}(1 - p^{i}_{tag}), \tag{8}$$

where p^{i}_{tag} is the probability for jet i in the event to have a b-tag. The probability for a b-tagged Monte Carlo jet originating from a b or c quark to have a b-tag in the data is the b-tag scale factor. The b-tag scale factor is the ratio of data to Monte Carlo b-tag efficiencies. It is estimated to be 0.95 ± 0.04 for secondary vertex tags [7] and 0.85 ± 0.07 for jet probability tags [22]. In the case where there are additional light-flavor jets produced in the W + heavy flavor events, there is a small chance for those light-flavor jets to be incorrectly tagged as b-jets. We account for this in Equation 8 by giving these just a small probability to be incorrectly tagged. We call the probability to be incorrectly tagged the mistag probability. It is discussed in detail in Section IV D.

Table VI shows the corrected heavy-flavor fractions for our W + heavy-flavor samples divided according to the heavy-flavor process and number of reconstructed jets. It is necessary to divide the samples by heavy-flavor process because b- and c-jets have different tagging efficiencies. Table VII shows the corrected per-event tagging efficiencies. We calculate the W + heavy-flavor normalizations using Eq. 6 and the fractions and efficiencies from the tables.

The two sources of uncertainties for the W + heavy-flavor backgrounds are the b-tag scale factor uncertainty and the heavy flavor fraction uncertainty. We accommodate the b-tag scale factor uncertainty by shifting the scale factor by $\pm 1\sigma$, propagating the change through our background calculation, and using difference between the shifted and nominal calculation as our error. We add this error in quadrature with the heavy-flavor fraction uncertainty and use the total error as a constraint on the background in our likelihood fit.

Corrected Heavy Flavor (HF) fraction (%) of inclusive W + jet events by jet multiplicity					
Process	Number of Jets matched to HF	Fraction of Events by Jet Multiplicity W + 2 jets	W + 3 jets	W + 4 jets	W + 5 jets
$Wb\bar{b}$	($1b$)	2.2 ± 0.88	3.5 ± 1.4	4.63 ± 1.8	5.5 ± 2.2
$Wb\bar{b}$	($2b$)	1.32 ± 0.52	2.6 ± 1.0	4.17 ± 1.7	6.0 ± 2.4
$Wc\bar{c}$	($1c$)	11 ± 4.4	14 ± 5.6	15.18 ± 6.1	15.8 ± 6.3
$Wc\bar{c}$	($2c$)	2.1 ± 0.84	4.7 ± 1.9	7.69 ± 3.1	10.9 ± 4.4

TABLE VI: The corrected fraction of inclusive W + jet events that contain heavy-flavor. The fractions are divided into separate categories according to the Monte Carlo flavor information for jets in the event and the number of reconstructed heavy-flavor jets. For example, $Wb\bar{b}$ ($1b$) events have two b-quarks at the generator level, but only one b-quark matched to a reconstructed jet. The fractions from ALPGEN Monte Carlo have been scaled by the data-derived calibration factor of 1.4 ± 0.4.

D. Mistagged Jets

W + light flavor events with a fake b-tag migrate into our signal region. Our estimate of the number of falsely tagged W+light flavor events is based on the pretag number of W + light flavor events and the sample mistag probability ϵ_{mistag} in equation 7. The sample mistag probability is based on the per-jet mistag probability. For each event in our W + light flavor Monte Carlo samples, we apply the per-jet mistag probability to each jet and combine the probabilities to get an event mistag probability. We combine the event mistag rates to get ϵ_{mistag}.

We estimate the per-jet mistag probability for each of our two tagging algorithms using a data sample of generic jets with at least two well-measured silicon tracks. The decay length is defined as the distance between the secondary vertex and the primary vertex in the plane perpendicular to the beam direction. This decay length is signed based on whether the tracks are consistent with the decay of a particle that was moving away from (positive sign) or towards (negative sign) the primary vertex. False tags are equally likely to have positive or negative decay lengths to first order. The symmetry allows calibration of the

Corrected Per-event b-tag efficiencies				
One SECVTX Tag Efficiency				
Jet Multiplicity	2 jets	3 jets	4 jets	5 jets
Event Eff ($1b$) (%)	23.10	24.68	25.02	27.14
Event Eff ($2b$) (%)	30.09	30.34	30.35	29.71
Event Eff ($1c$) (%)	7.02	7.69	8.68	10.24
Event Eff ($2c$) (%)	9.46	10.46	11.24	12.12
Two SECVTX Tag Efficiency				
Jet Multiplicity	2 jets	3 jets	4 jets	5 jets
Event Eff ($1b$) (%)	0.30	0.78	1.34	1.76
Event Eff ($2b$) (%)	8.76	9.68	10.18	11.14
Event Eff ($1c$) (%)	0.04	0.12	0.24	0.40
Event Eff ($2c$) (%)	0.38	0.55	0.88	0.91
One SECVTX TAG + One JETPROB Tag Efficiency				
Jet Multiplicity	2 jets	3 jets	4 jets	5 jets
Event Eff ($1b$) (%)	0.79	1.75	2.57	3.74
Event Eff ($2b$) (%)	6.95	7.78	8.86	9.77
Event Eff ($1c$) (%)	0.20	0.47	0.78	1.24
Event Eff ($2c$) (%)	1.19	1.59	2.14	2.43

TABLE VII: The corrected per-event tagging efficiencies for events with heavy-flavor content. The event efficiencies are divided into separate categories depending on the Monte Carlo truth flavor information for jets in the event: $1b$ events have one jet matched to b-quark, $2b$ events have two jets matched to a b-quark, $1c$ events have one jet matched to a c-quark, and $2c$ events have two jets matched to a c-quark.

false tag probability using negative tags. There is a slightly greater chance for a false tag to have a positive decay length due to material interaction, and our estimate accounts for this asymmetry. The false tag probability for SECVTX is parameterized in bins of η, number of vertices, jet E_T, track multiplicity, and the scalar sum of the total event E_T [21]. We parameterize jet probability mistaging in jet η, z position of primary vertex, jet E_T, track

multiplicity, and scalar sum of the total event E_T.

We estimate the uncertainties on the per-jet mistag probability by using negatively tagged jets in the data. The uncertainty estimates check for consistency between the number of expected and observed negative tags. The uncertainties are accounted for in the analysis by fluctuating the per-jet tag probabilities by $\pm 1\sigma$, and propagating the change through the background estimate.

E. Summary of Background Estimate

Tables VIII through XIII summarize our background estimate for our dataset of 2.7 fb^{-1}. Figures 3 through 5 present the information from the tables as plots. The plots show the background estimate compared to data. The largest errors on the background estimate come from the large uncertainty on the heavy flavor fraction used to calculate W + charm and W + bottom. We add these large uncertainties linearly because they come from the same source. The b-tagging scale factor uncertainty is also correlated across all backgrounds and added linearly. In general, the background estimate agrees with the data within uncertainties for each jet multiplicity. The agreement of the background estimate with the data in the high-jet-multiplicity bins gives us confidence that our estimate is correct in our two-jet search region.

CDF Run II 2.7 fb^{-1}				
Tight Lepton Background Prediction and Event Yields				
Events with Exactly One Secvtx Tag				
Process	2jets	3jets	4jets	5jets
All Pretag Candidates	38729	6380	1677	386
WW	40.6 ± 4.2	11.9 ± 1.2	2.92 ± 0.25	0.71 ± 0.06
WZ	13.86 ± 0.94	3.43 ± 0.23	0.93 ± 0.06	0.2 ± 0.02
ZZ	0.48 ± 0.04	0.19 ± 0.06	0.081 ± 0.007	0.023 ± 0.002
Top Pair	102 ± 14	193 ± 26	183 ± 26	59.4 ± 8.8
Single Top s-Channel	23.88 ± 2.2	6.95 ± 0.67	1.47 ± 0.15	0.28 ± 0.03
Single Top t-Channel	42.53 ± 4.4	9.24 ± 0.94	1.62 ± 0.17	0.22 ± 0.02
Z+Jets	28.72 ± 3.4	8.65 ± 0.96	2.73 ± 0.29	0.53 ± 0.06
W+bottom	365.6 ± 140	91.0 ± 35	19.4 ± 8	3.97 ± 1.7
W+charm	364.6 ± 140	81.2 ± 31	17.3 ± 7	3.64 ± 1.6
Mistags	319 ± 42	83.8 ± 13	18.8 ± 5.07	3.82 ± 1.5
Non-W	107 ± 43	40.2 ± 17	17.3 ± 14	4.48 ± 4.4
Total Prediction	1408 ± 287	530 ± 75	266 ± 34	77 ± 11
Observed	1404	486	281	81

TABLE VIII: Background summary table for events with a central lepton and exactly one secondary vertex tag. The heavy-flavor fraction F_{HF} is the source of the large correlated uncertainty for W+bottom and W+charm. The other large source of correlated uncertainty is the b-tagging scale factor.

CDF Run II 2.7 fb^{-1}				
Isolated Track Background Prediction and Event Yields				
Events with Exactly One Secvtx Tag				
Process	2jets	3jets	4jets	5jets
All Pretag Candidates	4253	1380	427	117
WW	6.4 ± 0.65	2.83 ± 0.25	0.75 ± 0.07	0.23 ± 0.02
WZ	2.41 ± 0.16	0.92 ± 0.06	0.19 ± 0.01	0.063 ± 0.005
ZZ	0.127 ± 0.009	0.052 ± 0.004	0.007 ± 0.001	0.006 ± 0.001
Top Pair	28.0 ± 3.8	58.3 ± 8.0	53.4 ± 7.6	16.8 ± 2.5
Single Top s-Channel	6.08 ± 0.58	1.91 ± 0.19	0.43 ± 0.04	0.08 ± 0.01
Single Top t-Channel	10.1 ± 1.1	2.32 ± 0.24	0.41 ± 0.05	0.07 ± 0.01
Z+Jets	9.05 ± 1.1	3.35 ± 0.36	0.74 ± 0.077	0.16 ± 0.02
W+bottom	39.9 ± 16	18.4 ± 7.3	5.35 ± 2.3	1.91 ± 0.79
W+charm	36.7 ± 15	16.2 ± 6.5	4.66 ± 2.0	1.53 ± 0.64
Mistags	43.2 ± 8.2	17.7 ± 4.0	4.81 ± 1.7	1.82 ± 0.64
Non-W	37.6 ± 15	22.2 ± 8.9	5.26 ± 4.2	2.13 ± 1.7
Total Prediction	220 ± 35	144 ± 19	76 ± 10	25 ± 3.4
Observed	208	150	78	31

TABLE IX: Background summary table for events with an isolated track and exactly one secondary vertex tag . The heavy-flavor fraction F_{HF} is the source of the large correlated uncertainty for W+bottom and W+charm. The other large source of correlated uncertainty is the b-tagging scale factor.

CDF Run II 2.7 fb^{-1}				
Tight Lepton Background Prediction and Event Yields				
Events with One Secvtx Tag and One Jet Prob Tag				
Process	2jets	3jets	4jets	5jets
All Pretag Candidates	44723	7573	1677	386
WW	1.24 ± 0.53	0.85 ± 0.31	0.4 ± 0.13	0.165 ± 0.047
WZ	2.51 ± 0.43	0.78 ± 0.16	0.18 ± 0.04	0.052 ± 0.013
ZZ	0.098 ± 0.017	0.053 ± 0.009	0.021 ± 0.004	0.005 ± 0.001
Top Pair	20.4 ± 4.2	63.9 ± 13	79.3 ± 16	29.9 ± 6.1
Single Top s-Channel	6.99 ± 1.1	2.45 ± 0.42	0.57 ± 0.1	0.133 ± 0.024
Single Top t-Channel	2.1 ± 0.64	1.67 ± 0.36	0.46 ± 0.09	0.076 ± 0.015
Z+Jets	1.81 ± 0.54	1.17 ± 0.35	0.34 ± 0.12	0.1 ± 0.03
W+bottom	49.1 ± 20	17.1 ± 7.2	4.89 ± 2.1	1.28 ± 0.59
W+charm	18.0 ± 8.3	7.89 ± 3.7	2.57 ± 1.2	0.67 ± 0.34
Mistags	5.84 ± 6.0	3.01 ± 3.4	0.1 ± 1.1	0.29 ± 0.37
Non-W	11.1 ± 5.33	6.57 ± 3.5	3.38 ± 3.4	1.51 ± 2.1
Total Prediction	119 ± 30	105 ± 19	93 ± 17	34 ± 7
Observed	124	109	101	36

TABLE X: Background summary table for events with a central lepton and two tags: one secondary vertex tag and one jet probability tag. The heavy-flavor fraction F_{HF} is the source of the large correlated uncertainty for W+bottom and W+charm. The other large source of correlated uncertainty is the b-tagging scale factor.

CDF Run II 2.7 fb^{-1}				
Isolated Track Background Prediction and Event Yields				
Events with One Secvtx Tag, One Jet Prob Tag				
Process	2jets	3jets	4jets	5jets
All Pretag Candidates	5149	1623	487	124
WW	0.2 ± 0.09	0.24 ± 0.09	0.1 ± 0.03	0.03 ± 0.01
WZ	0.51 ± 0.09	0.2 ± 0.04	0.048 ± 0.01	0.013 ± 0.004
ZZ	0.032 ± 0.006	0.021 ± 0.005	0.007 ± 0.001	0.002 ± 0.001
Top Pair	6.44 ± 1.3	20.0 ± 4.2	24.6 ± 4.9	8.98 ± 1.8
Single Top s-Channel	1.93 ± 0.31	0.74 ± 0.13	0.19 ± 0.03	0.043 ± 0.009
Single Top t-Channel	0.53 ± 0.16	0.5 ± 0.11	0.12 ± 0.03	0.028 ± 0.005
Z+Jets	0.61 ± 0.2	0.41 ± 0.13	0.13 ± 0.04	0.039 ± 0.013
W+bottom	6.0 ± 2.7	3.4 ± 1.6	1.37 ± 0.67	0.59 ± 0.26
W+charm	2.14 ± 1.07	1.64 ± 0.86	0.77 ± 0.41	0.34 ± 0.17
Mistags	0.8 ± 1.18	0.61 ± 0.84	0.27 ± 0.31	0.13 ± 0.17
Non-W	1.97 ± 0.79	1.38 ± 0.55	0.99 ± 0.79	0.37 ± 0.5
Total Prediction	21 ± 4	29 ± 5	29 ± 5	11 ± 2
Observed	21	30	32	12

TABLE XI: Background summary table for events with an isolated track and two tags: one secondary vertex tag and one jet probability tag. The heavy-flavor fraction F_{HF} is the source of the large correlated uncertainty for W+bottom and W+charm. The other large source of correlated uncertainty is the b-tagging scale factor.

CDF Run II 2.7 fb^{-1}				
Tight Lepton Background Prediction and Event Yields				
Events with Two Secvtx Tags				
Process	2jets	3jets	4jets	5jets
All Pretag Candidates	44723	7573	1677	386
WW	0.3 ± 0.06	0.29 ± 0.05	0.17 ± 0.03	0.08 ± 0.01
WZ	3.32 ± 0.37	0.94 ± 0.11	0.19 ± 0.02	0.04 ± 0.01
ZZ	0.1 ± 0.01	0.073 ± 0.008	0.019 ± 0.002	0.005 ± 0.001
Top Pair	25.9 ± 4.2	76.8 ± 12	101 ± 16	36.1 ± 5.9
Single Top s-Channel	9.55 ± 1.2	3.25 ± 0.41	0.72 ± 0.09	0.15 ± 0.02
Single Top t-Channel	2.15 ± 0.3	1.9 ± 0.26	0.53 ± 0.07	0.1 ± 0.01
Z+Jets	1.42 ± 0.2	0.95 ± 0.13	0.26 ± 0.04	0.085 ± 0.013
W+bottom	55.0 ± 22	18.1 ± 7.4	4.88 ± 2.0	1.24 ± 0.55
W+charm	4.87 ± 2.0	2.35 ± 1	0.94 ± 0.4	0.25 ± 0.12
Mistags	1.38 ± 0.39	0.93 ± 0.3	0.34 ± 0.12	0.11 ± 0.05
Non-W	8.96 ± 4.0	5.02 ± 2.0	0.74 ± 1.6	0.23 ± 1.5
Total Prediction	113 ± 25	111 ± 16	110 ± 17	38 ± 6
Observed	114	132	104	42

TABLE XII: Background summary table for events with a central lepton and two secondary vertex tags. The heavy-flavor fraction F_{HF} is the source of the large correlated uncertainty for W+bottom and W+charm. The other large source of correlated uncertainty is the b-tagging scale factor.

CDF Run II 2.7 fb^{-1}				
Isolated Track Background Prediction and Event Yields				
Events with Two Secvtx Tags				
Process	2jets	3jets	4jets	5jets
All Pretag Candidates	5149	1623	487	124
WW	0.036 ± 0.008	0.13 ± 0.02	0.067 ± 0.012	0.019 ± 0.003
WZ	0.65 ± 0.07	0.24 ± 0.03	0.029 ± 0.003	0.01 ± 0.001
ZZ	0.045 ± 0.005	0.025 ± 0.003	0.01 ± 0.001	0.002 ± 0
Top Pair	7.75 ± 1.2	22.7 ± 3.7	31.5 ± 5.1	11.5 ± 1.9
Single Top s-Channel	2.66 ± 0.34	0.91 ± 0.12	0.21 ± 0.03	0.045 ± 0.006
Single Top t-Channel	0.58 ± 0.08	0.57 ± 0.08	0.18 ± 0.02	0.035 ± 0.005
Z+Jets	0.51 ± 0.07	0.32 ± 0.05	0.093 ± 0.014	0.025 ± 0.004
W+bottom	7.51 ± 3.3	3.59 ± 1.63	1.41 ± 0.66	0.53 ± 0.23
W+charm	0.68 ± 0.3	0.56 ± 0.26	0.26 ± 0.13	0.18 ± 0.05
Mistags	0.27 ± 0.13	0.2 ± 0.1	0.089 ± 0.05	0.052 ± 0.026
Non-W	1.78 ± 0.71	1.89 ± 0.76	6.53 ± 5.2	2.65 ± 2.1
Total Prediction	22 ± 4	31 ± 4	40 ± 7	15 ± 3
Observed	24	31	37	15

TABLE XIII: Background summary table for events with an isolated track and two secondary vertex tags. The heavy-flavor fraction F_{HF} is the source of the large correlated uncertainty for W+bottom and W+charm. The other large source of correlated uncertainty is the b-tagging scale factor.

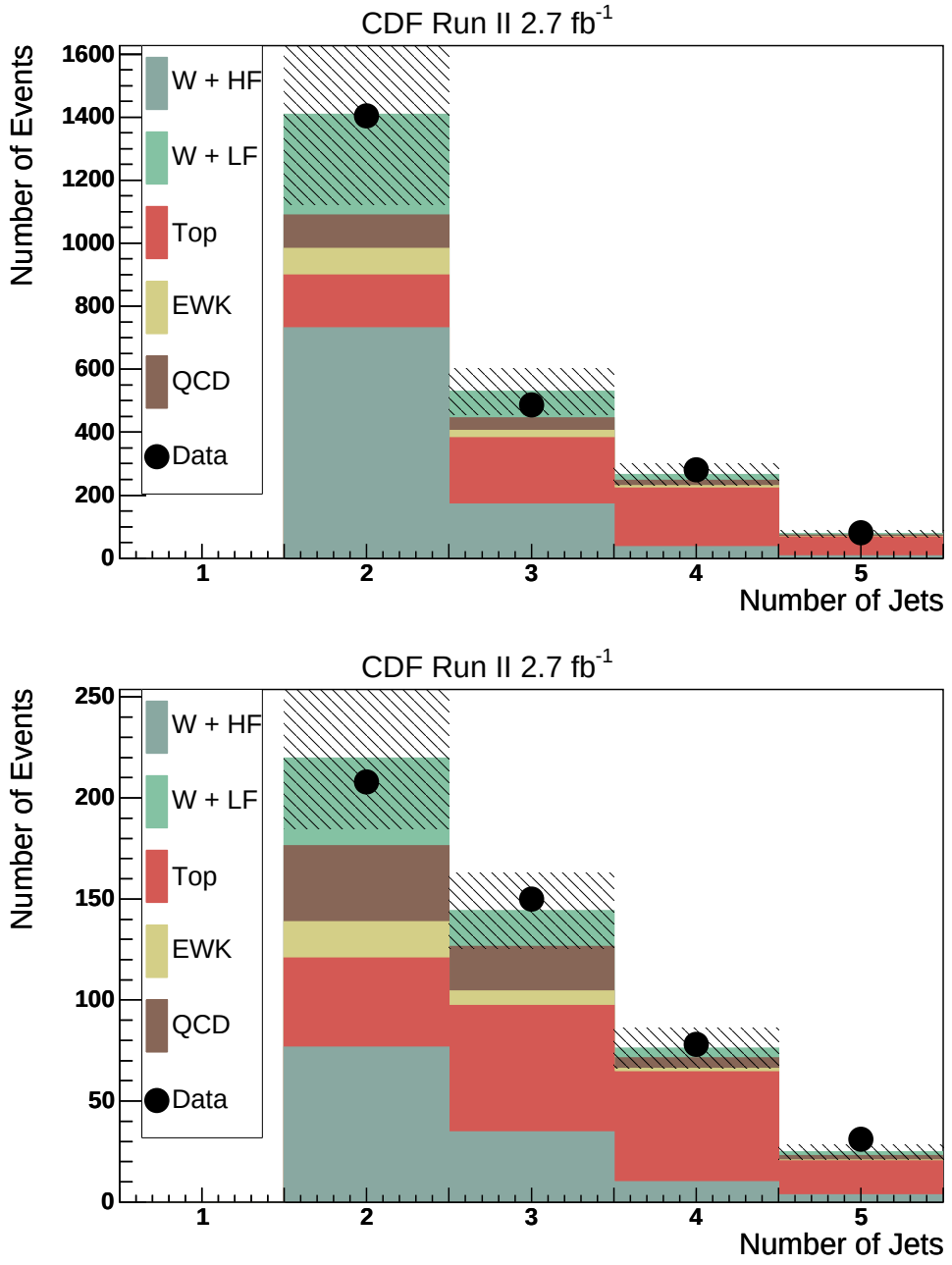

FIG. 3: Number of expected and observed background events for events with exactly one SECVTX tag, shown as a function of jet multiplicity. The plots show tight leptons (top) and isolated tracks (bottom). The hatched regions indicate the total uncertainty.

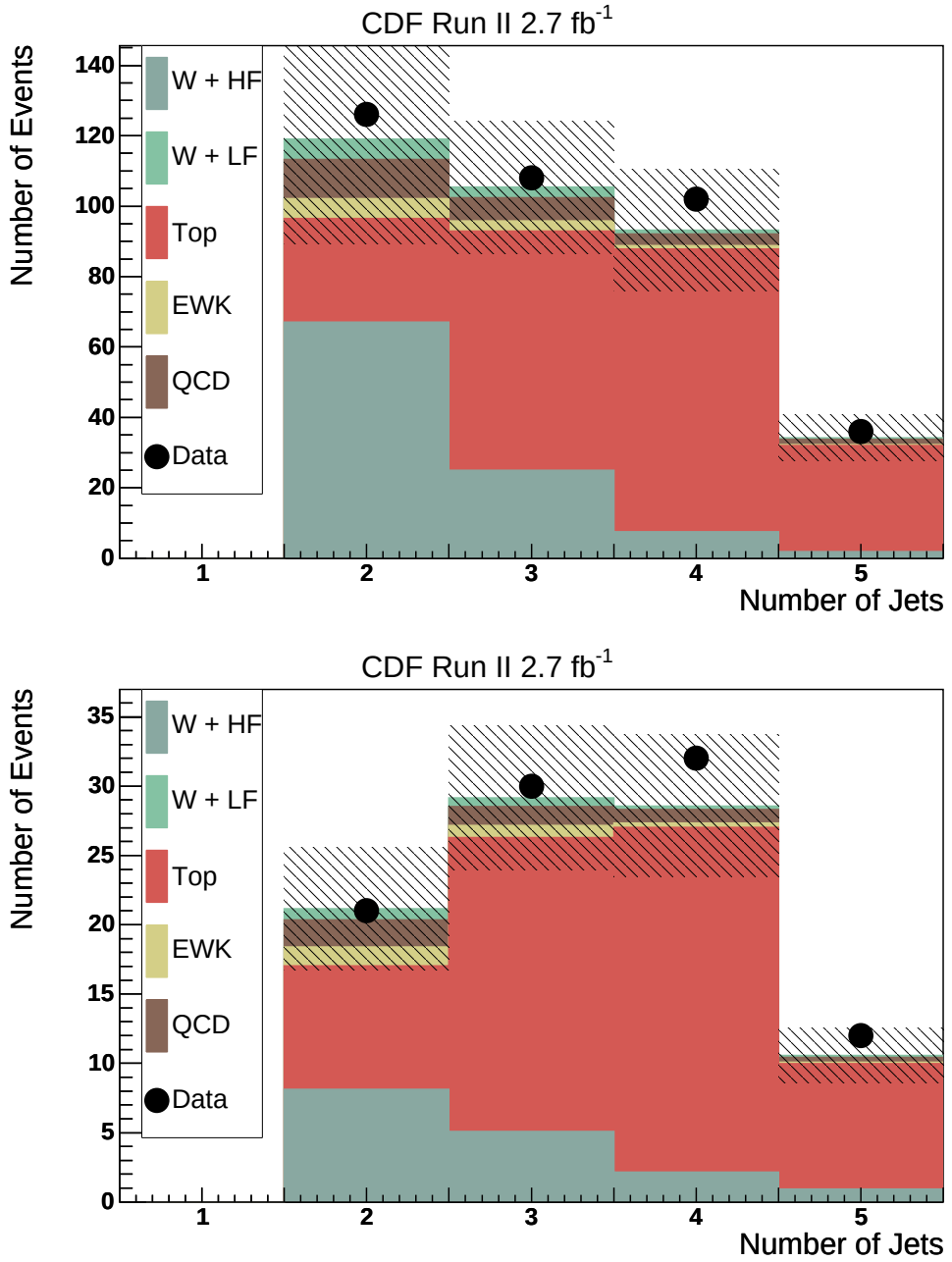

FIG. 4: Number of expected and observed background events for events with one SECVTX tag and one jetprob tag, shown as a function of jet multiplicity. The plots show tight leptons (top) and isolated tracks (bottom).The hatched regions indicate the total uncertainty.

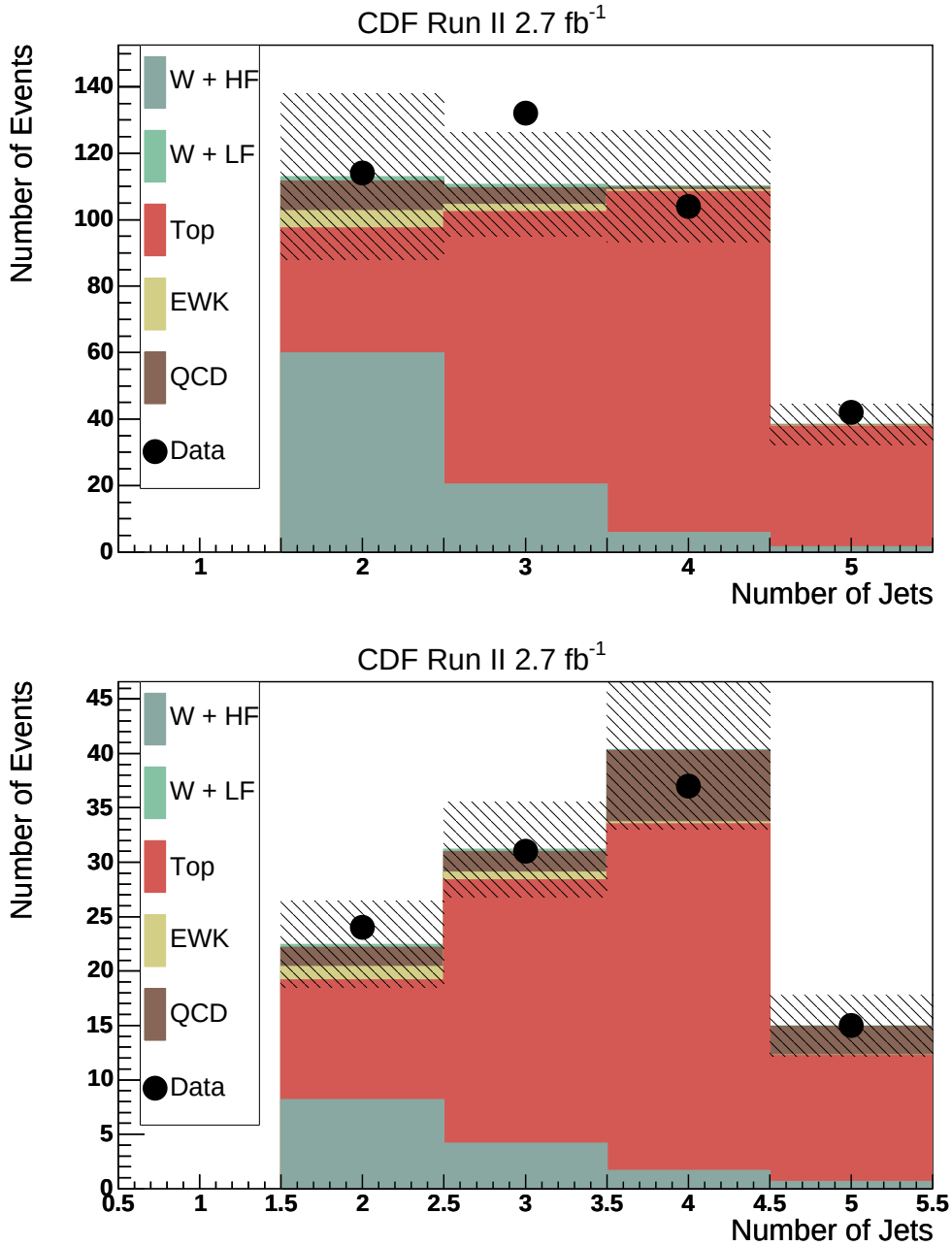

FIG. 5: Number of expected and observed background events for events with two SECVTX tags, shown as a function of jet multiplicity. The plots show tight leptons (top) and isolated tracks (bottom).The hatched regions indicate the total uncertainty.

V. HIGGS BOSON SIGNAL ACCEPTANCE

We simulated the WH signal kinematics using the PYTHIA Monte Carlo program [31]. We generated signal Monte Carlo samples for Higgs masses between 100 and 150 GeV/c^2. The number of expected $WH \to \ell\nu b\bar{b}$ events, N, is given by:

$$N = \epsilon \cdot \int \mathcal{L}dt \cdot \sigma(p\bar{p} \to WH) \cdot \mathcal{B}(H \to b\bar{b}), \tag{9}$$

where ϵ, $\int \mathcal{L}dt$, $\sigma(p\bar{p} \to WH)$, and $\mathcal{B}(H \to b\bar{b})$ are the event detection efficiency, integrated luminosity, production cross section, and branching ratio, respectively. The production cross section and branching ratio are calculated to next-to-leading order (NLO) precision [4].

The total event detection efficiency is composed of several efficiencies: the primary vertex reconstruction efficiency, the trigger efficiency, the lepton identification efficiency, the b-tagging efficiency, and the event selection efficiency [5]. Each efficiency is calibrated to match observations.

We parametrize the $\not\!\!E_T$ trigger turn-on as a function of $\not\!\!E_T^{\text{vertex}}$, which is $\not\!\!E_T$ corrected for the primary vertex position but not muons or jet energy scale corrections. We use $\not\!\!E_T^{\text{vertex}}$ because it is close to the $\not\!\!E_T$ calculation used by the trigger and is modeled better in the Monte Carlo than $\not\!\!E_T^{\text{raw}}$, which is calculated assuming $z_0 = 0$. The measurement of the jets can influence the measurement of the $\not\!\!E_T$. We require that the jets in the event are above the trigger threshold ($E_T > 25$ GeV) and well separated ($\Delta R > 1.0$), which reduces the impact of the jets on the $\not\!\!E_T$. We measured the turn-on curve using events recorded with the CMUP trigger, which is independent from the $\not\!\!E_T$ + 2 jets trigger. We selected events passing our jet requirements, and measured their efficiency to pass the $\not\!\!E_T$ + 2 jets trigger as a function of $\not\!\!E_T^{\text{vertex}}$. Figure 6 shows the measured $\not\!\!E_T$ + 2 jets trigger turn-on. We use the parmeterized turn-on curve to weight each Monte Carlo event according to its efficiency to pass the trigger.

The expected number of signal events is estimated by equation 9 at each Higgs boson mass point. Table XIV shows the number of expected WH events for $M_H = 120$ GeV/c^2 in 2.7 fb^{-1}.

The total systematic uncertainty on the acceptance comes from several sources, including the jet energy scale, initial and final state radiation, lepton identification, trigger efficiencies, and b-tagging scale factor. The largest uncertainties come from the b-tagging scale factor uncertainty and isolated track identification uncertainty.

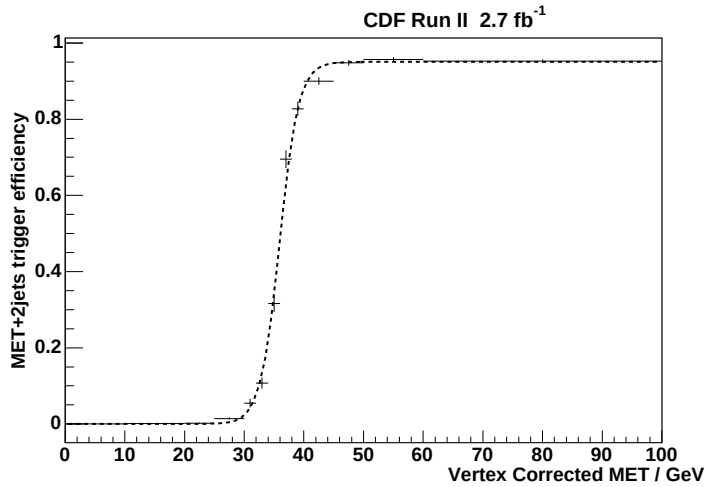

FIG. 6: $\not\!\!E_T$ plus jets trigger turn-on curve parameterized as a function of vertex $\not\!\!E_T$. The plot shows the turn-on curve measured in 2.7 fb^{-1} of CDF data.

We assign a 2% uncertainty to the CEM, CMUP, and CMX lepton identification efficiency, and an 8% uncertainty to isolated track identification. The identification uncertainties are based on studies comparing Z boson events in data and Monte Carlo.

The high p_T lepton triggers have a 1% uncertainty on their efficiencies. We measure the trigger efficiency uncertainty by using backup trigger paths or Z boson events. We measure a 3% uncertainty for events collected on the $\not\!\!E_T$ + 2 jets trigger by examining the variations in the $\not\!\!E_T$ turn-on curve in sub-samples with kinematics different from the average sample. We use the variation in the $\not\!\!E_T$ turn-on to calculate a variation in signal acceptance, and we use the mean variation in signal acceptance as our uncertainty.

We estimate the impact of changes in initial and final state radiation by halving and doubling the parameters related to ISR and FSR in the Monte Carlo event generation [32]. The difference from the nominal acceptance is taken as the systematic uncertainty.

The uncertainty in the incoming partons' energies relies on the the parton distribution function (PDF) fits. A NLO version of the PDFs, CTEQ6M, provides a 90% confidence interval of each eigenvector [33]. The nominal PDF value is reweighted to the 90% confidence level value, and the corresponding reweighted acceptance is computed. The differences between the nominal and the reweighted acceptances are added in quadrature, and the total is assigned as the systematic uncertainty [7].

CDF Run II 2.7 fb^{-1}	
Number of Expected WH (M_H = 120 GeV/c^2) Events	
Lepton Type	Expected Number of WH events
Exactly One Secvtx Tag	
CEM	1.58 ± 0.08
CMUP	0.91 ± 0.05
CMX	0.44 ± 0.02
ISOTRK	0.72 ± 0.07
Total	3.65 ± 0.22
Two Secvtx Tags	
CEM	0.66 ± 0.07
CMUP	0.37 ± 0.04
CMX	0.17 ± 0.02
ISOTRK	0.36 ± 0.05
Total	1.56 ± 0.18
One Secvtx Tag and One Jet Probability Tag	
CEM	0.48 ± 0.05
CMUP	0.26 ± 0.03
CMX	0.13 ± 0.01
ISOTRK	0.23 ± 0.03
Total	1.10 ± 0.12

TABLE XIV: Expected number of WH events at a M(H)=120, shown separately for different tag categories and lepton types. The lepton types are categorized based on the sub-detector regions.

The uncertainty due to the jet energy scale uncertainty (JES) [14] is calculated by shifting jet energies in WH Monte Carlo samples by $\pm 1\sigma$. The deviation from the nominal acceptance is taken as the systematic uncertainty.

The systematic uncertainty on the b-tagging efficiency is based on the scale factor uncertainty discussed in Sec. IV C. The total systematic uncertainties for various b-tagging options and lepton categories are summarized in Table XV.

Source	Uncertainty (%)		
	Two Secvtx Tags	One Secvtx One JetProb tag	Exactly One Secvtx
Trigger Lepton (Isotrk) ID	∼2% (8.85%)	∼2% (8.85%)	∼2% (8.85%)
Lepton (MET+Jets) Trigger	<1% (3%)	<1% (3%)	<1% (3%)
ISR/FSR	5.2%	4.0%	2.9%
PDF	2.1%	1.5%	2.3%
JES	2.5%	2.8%	1.2%
b-tagging	8.4%	9.1%	3.5%
Total (Isotrk)	10.6% (13.8%)	10.5% (14.0%)	5.6% (10.1%)

TABLE XV: Systematic uncertainty on the WH acceptance. "ST+ST" refers to double secondary vertex tagged events while "ST+JP" refers to secondary vertex plus jet probability tagged events. Effects of limited Monte Carlo statistics are included in these values.

VI. NEURAL NETWORK DISCRIMINANT

To further improve the signal to background discrimination after event selection, we employ an artificial neural network (NN). Neural networks offer an advantage over a single-variable discriminants because they combine information from several kinematic variables. Our neural network is trained to distinguish W+Higgs boson events from backgrounds. We employ the same neural network that was used to obtain the 1.9 fb^{-1} result [5]. The following section reviews its main features.

Our neural network configuration has 6 input variables, 11 hidden nodes, and 1 output node. The input variables were selected by an iterative network optimization procedure from a list of 76 possible variables. The optimization procedure identified the most sensitive one-variable NN, then looped over all remaining variables and found the most sensitive two-variable NN. The process continued until adding a new variable does not improve sensitivity by more than 0.5 percent. The 6 inputs are:

M_{jj+}**:** The dijet mass plus is the invariant mass calculated from the two reconstructed jets. If there are additional loose jets present, where loose jets have $E_T > 12$ GeV, $|\eta| < 2.4$ and have a centroid within $\Delta R < 0.9$ of one of the leading jets, then the loose jet that is closest to one of the two jets is included in this invariant mass calculation.

$\sum E_T$**(Loose Jets):** This variable is the scalar sum of the loose jet transverse energies.

p_T **Imbalance:** This variable expresses the difference between $\not\!\!E_T$ and the scalar sum of the transverse momenta of the lepton and the jets. Specifically, it is calculated as $P_T(jet_1) + P_T(jet_2) + P_T(lep) - \not\!\!E_T$.

$M_{l\nu j}^{min}$**:** This is the invariant mass of the lepton, $\not\!\!E_T$, and one of the two jets, where the jet is chosen to give the minimum invariant mass. For this quantity, the p_z component of the neutrino is ignored.

ΔR**(lepton-**ν_{max}**):** This is the ΔR separation between the lepton and the neutrino. We calculate the p_z of the neutrino by constraining the lepton and the $\not\!\!E_T$ to the W mass (80.42 GeV/c^2). The constraint produces a quadratic equation for p_Z and we choose the larger solution.

$P_T(W + H)$**:** This is the total transverse momentum of the W plus two jets system, $P_T(\vec{lep} + \vec{\nu} + \vec{jet}_1 + \vec{jet}_2)$.

The strongest discriminating variable in the neural network is the dijet mass plus.

We train our neural network with W+jets, $t\bar{t}$, single top, and WH signal Monte Carlo. We do not use QCD events to train our neural network. We use the same topology and input variables to train separate neural networks for each Higgs signal Monte Carlo sample. The samples range from $M(H) = 100$ to 150 GeV/c^2 in 5 GeV increments. At each Higgs mass, we use the same neural network for tight lepton and isolated track events.

Figures 7 through 9 show the six neural network input variables for isolated track events in the pretag control region. The plots show that our background model describes the data reasonably for all the neural network input variables. The modeling is not ideal in regions that have a large amount of QCD, such as the region around $\Delta R_{MAX}(MET, l) = 2.5$ in Figure 9 and the region around $M_{l\nu j}^{min} = 50$ in Figure 8. Figures 10 through 12 show that these differences are less significant after removing some of the QCD contamination with b-tagging. The hashed region in Figures 10 through 12 indicates uncertainty on the background estimate. Taking into account the uncertainty on the background estimate, this modeling is reasonable for the isolated track neural network input variables.

We studied the impact of QCD shape modeling in the tight lepton sample. We did not expect the QCD shape to have a large impact on the sensitivity because the neural

network was not trained with QCD events. We found that the large QCD normalization uncertainty (40%) accounted for the small variations that arose from using an alternative QCD model with different kinematics. Based on the tight lepton studies, we assume that the impact of QCD shape modeling on isolated track sample is also small compared to the QCD normalization uncertainty. This is not an aggressive assumption since the isolated track sample only accounts for 20% of the total sensitivity.

The tight lepton categories also show good agreement with the previous publication [5].

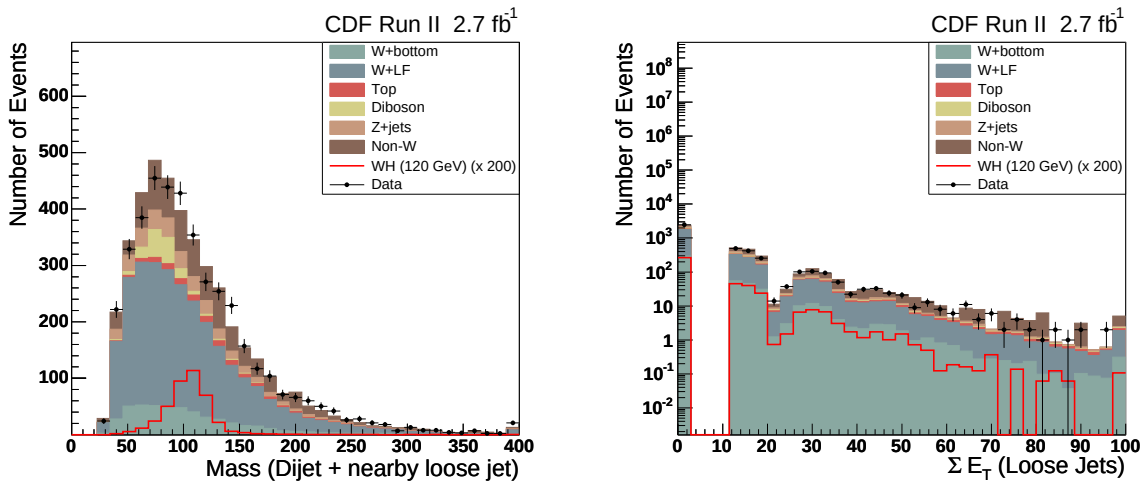

FIG. 7: Neural network input distributions for isolated track $W+2$ jet events in the pretag control region. The distributions shown are M_{jj+} (left) and $\sum E_T$(Loose Jets) (right). The differences in shape are attributable to QCD and are less significant in our higher-purity search regions.

VII. LIMIT ON HIGGS BOSON PRODUCTION RATE

We search for an excess of Higgs signal events in our neural network output distributions using a binned likelihood technique. Figures 13 through 15 show the neural network output distributions for events in different lepton and tag categories. We use the same likelihood expression and maximization technique as the prior CDF result [5] and described in [34]. We maximize the likelihood, fitting for a combination of Higgs signal plus backgrounds. We find no evidence for a Higgs boson signal in our sample, and so we set 95% confidence level upper limits on the WH cross section times branching ratio: $\sigma(p\bar{p} \to W^{\pm}H) \cdot \mathcal{B}(H \to b\bar{b})$. We compare our observed limits to our expected sensitivity by creating pseudo-experiments with

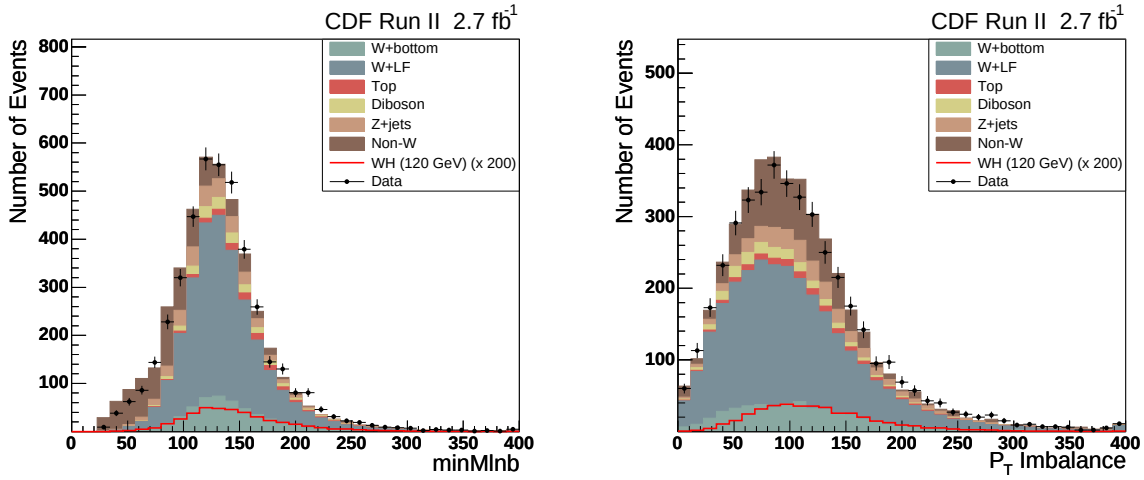

FIG. 8: Neural network input distributions for isolated track $W+2$ jet events in the pretag control region. The distributions shown are $M_{l\nu j}^{min}$ (left) and P_T Imbalance (right). The differences in shape are attributable to QCD and are less significant in our higher-purity search regions.

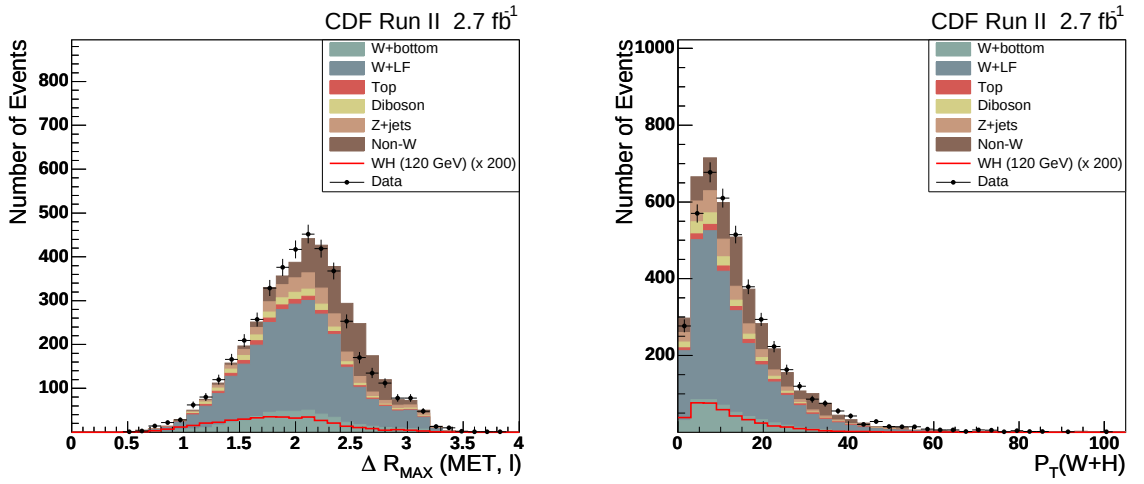

FIG. 9: Neural network input distributions for isolated track $W+2$ jet events in the pretag control region. The distributions shown are ΔR(lepton-ν_{max}) (left), $P_T(W+H)$ (right). The differences in shape are attributable to QCD and are less significant in our higher-purity search regions.

pseudo-data constructed from a sum of background templates. Our expected and observed limits are shown in Fig. 16 and Table XVI. The limits are expressed as a function of the Higgs boson mass hypothesis.

The likelihood technique accommodates the uncertainties on our background estimate

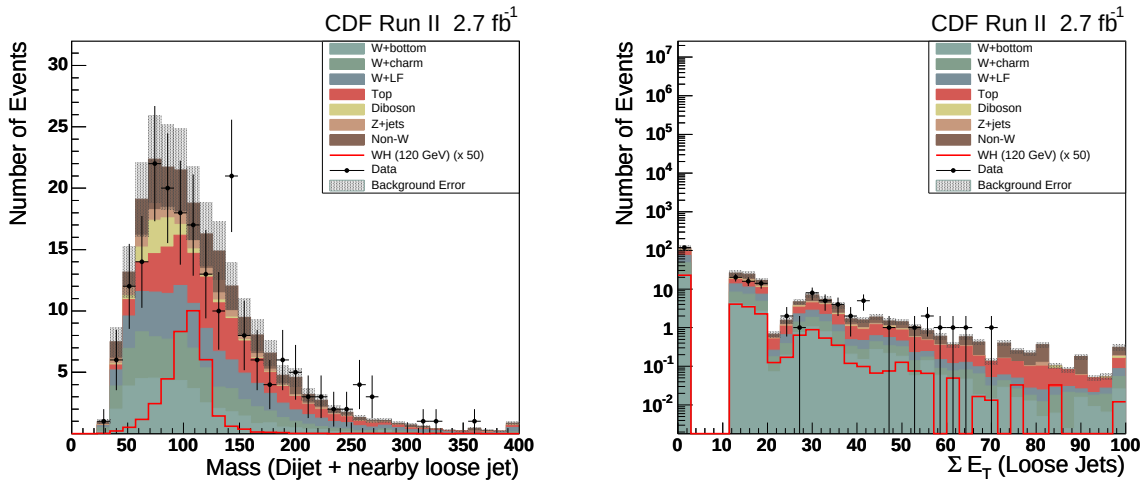

FIG. 10: Neural network input distributions for isolated track $W+2$ jet events in the one SECVTX tag region. The distributions shown are M_{jj+} (left) and $\sum E_T$(Loose Jets) (right). The differences in the shape are consistent with the uncertainty on our QCD model.

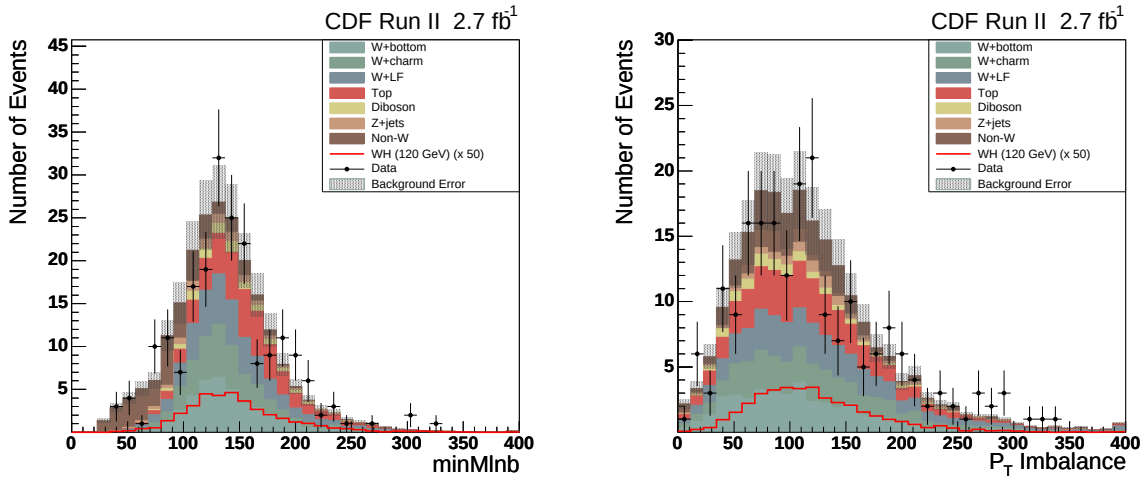

FIG. 11: Neural network input distributions for isolated track $W+2$ jet events in the one SECVTX region. The distributions shown are $M_{l\nu j}^{min}$ (left) and P_T Imbalance (right). The differences in the shape are consistent with the uncertainty on our QCD model.

by letting the overall background prediction float within Gaussian constraints. We use a different set of background and signal neural network template shapes for each combination of lepton type and tag category as a separate channel in the likelihood. We correlate the systematic uncertainties appropriately across different lepton types and tag categories.

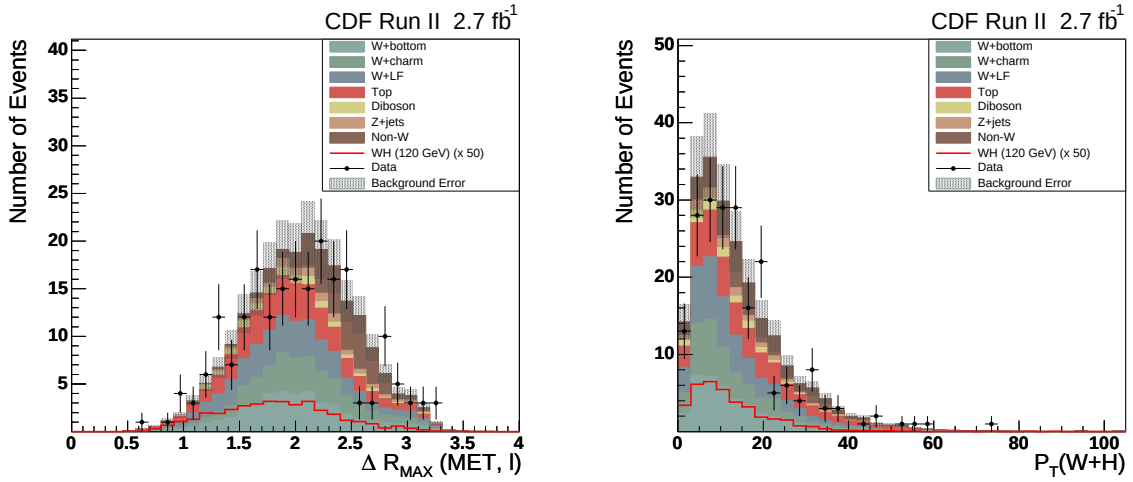

FIG. 12: Neural network input distributions for isolated track $W+2$ jet events in the one SECVTX region. The distributions shown are ΔR(lepton-ν_{max}) (left), $P_T(W+H)$ (right). The differences in the shape are consistent with the uncertainty on our QCD model.

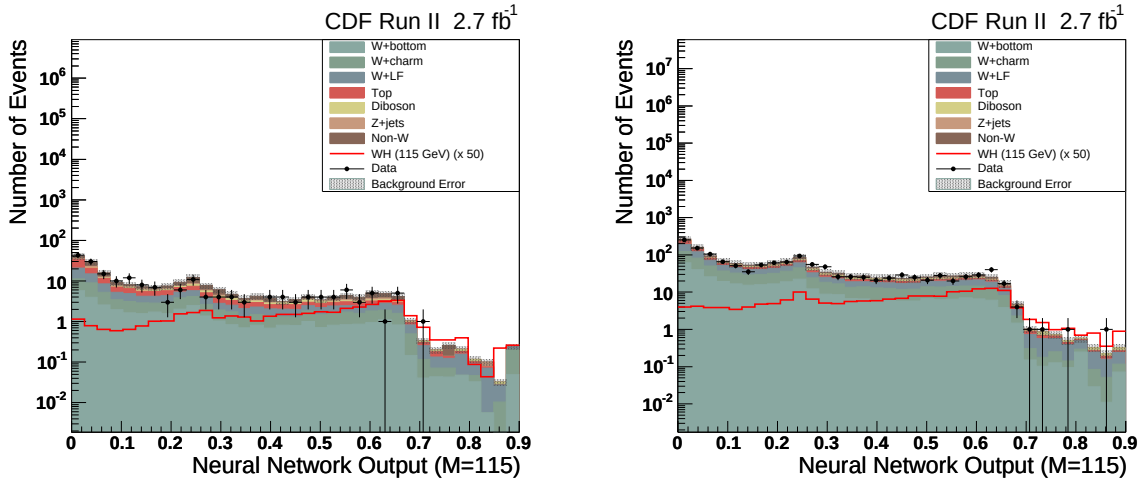

FIG. 13: Neural Network output distributions for events with one Secvtx tag. The neural network output is close to zero for "background-like" events, and close to one for "signal-like" events. The open red curve shows the expected distribution of WH Monte Carlo events. The WH expected curve is normalized to 50 times the standard model expectation. The plots show isolated track events (left) and lepton triggered events (right).

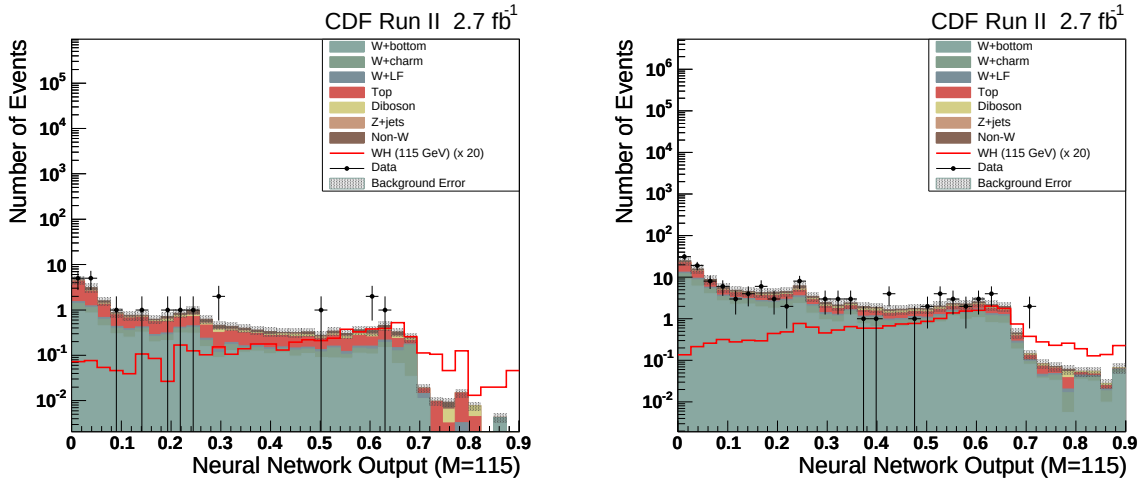

FIG. 14: Neural Network output distributions for events with one secvtx tag and one jet probability tag. The neural network output is close to zero for "background-like" events, and close to one for "signal-like" events. The open red curve shows the expected distribution of WH Monte Carlo events. The WH expected curve is normalized to 50 times the standard model expectation. The plots show isolated track events (left) and lepton triggered events (right).

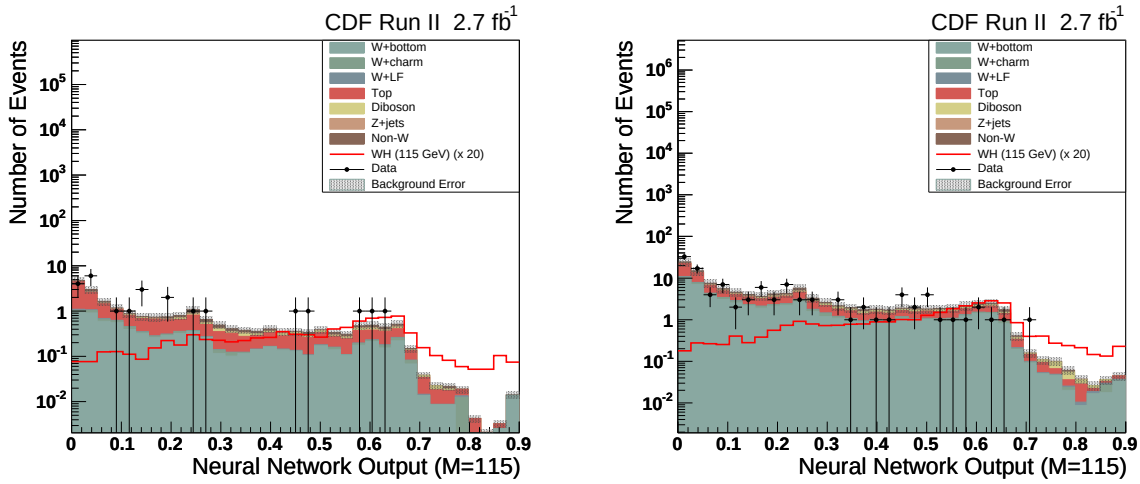

FIG. 15: Neural Network output distributions for events with two secvtx tags. The neural network output is close to zero for "background-like" events, and close to one for "signal-like" events. The open red curve shows the distribution of WH events. The WH curve is normalized to 50 times the standard model expectation. The plots show isolated track events (left) and lepton triggered events (right).

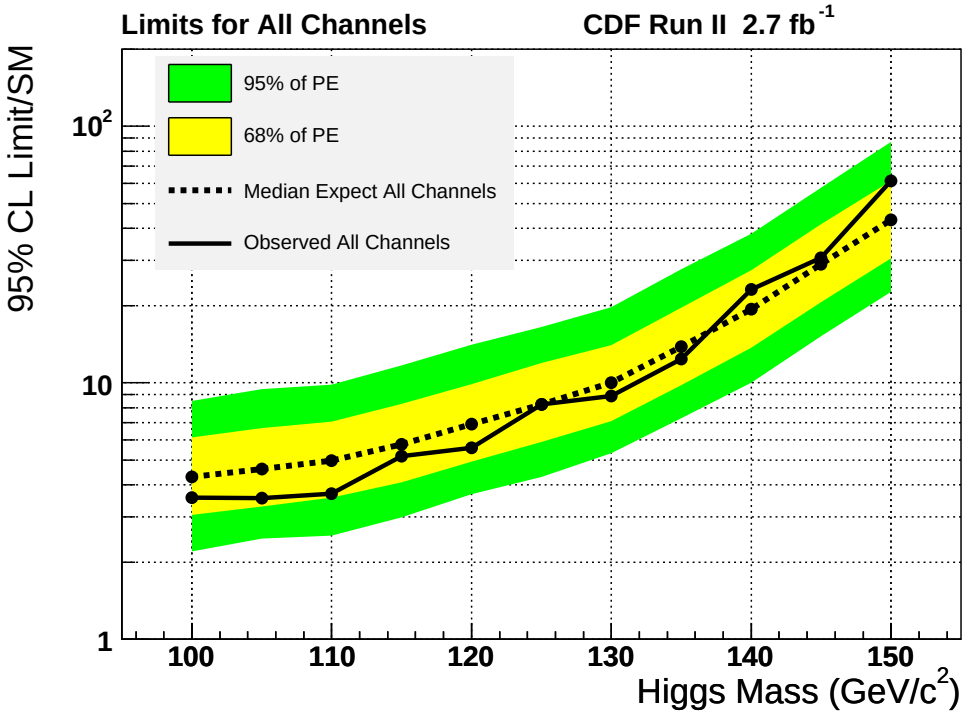

FIG. 16: 95% confidence level upper limit on $\sigma(p\bar{p} \to WH) \cdot \mathcal{B}(H \to b\bar{b})$, expressed as a ratio to the standard model expectation. The limits were obtained using an integrated luminosity of 2.7 fb^{-1} and analyzing both lepton triggered and $\not\!\!E_T$ + 2 jet triggered events. The dashed line indicates the median expected limit. The yellow and green regions encompass the limits in 68% and 95% of pseudo-experiments, respectively. The solid line shows the observed limits.

VIII. CONCLUSIONS

Our limit on WH production improves on the previous result by using more integrated luminosity and extending the lepton identification with isolated tracks. The increase in luminosity from 1.9 fb^{-1} to 2.7 fb^{-1} increases the sensitivity by ∼20%. Using isolated track events provides a ∼25% increase in acceptance above the prior analysis. The new isolated track events combined with minor improvements in background rejection yield a overall ∼15% increase in estimated sensitivity. Our expected limits are expressed as a ratio to the standard model production rate. The expected limits vary from 4.3 to 43.2 for Higgs masses from 100 to 150 GeV/c^2, respectively. We find no evidence for Higgs production in the data, and set observed limits at 3.6 to 61.1 for Higgs masses from 100 to 150 GeV/c^2, respectively.

CDF Run II Preliminary 2.7 fb^{-1} Limits for Combined Lepton and Tag Categories in units of SM cross sections		
M(H)	Observed Limit (x SM)	Expected Limit (x SM)
100	3.6	4.3
105	3.6	4.6
110	3.7	5.0
115	5.2	5.8
120	5.6	6.9
125	8.2	8.2
130	8.9	10.0
135	12.4	13.8
140	23.1	19.4
145	30.6	28.9
150	61.1	43.2

TABLE XVI: Expected and observed limits as a function of Higgs mass for the combined search of Tight Lepton and Isotrk events, including all tag categories. The limits are expressed in units of Standard Model WH cross sections.

Acknowledgments

We thank the Fermilab staff and the technical staffs of the participating institutions for their vital contributions. This work was supported by the U.S. Department of Energy and National Science Foundation; the Italian Istituto Nazionale di Fisica Nucleare; the Ministry of Education, Culture, Sports, Science and Technology of Japan; the Natural Sciences and Engineering Research Council of Canada; the National Science Council of the Republic of China; the Swiss National Science Foundation; the A.P. Sloan Foundation; the Bundesministerium für Bildung und Forschung, Germany; the Korean World Class University Program, the National Research Foundation of Korea; the Science and Technology Facilities Council and the Royal Society, UK; the Institut National de Physique Nucleaire et Physique des Particules/CNRS; the Russian Foundation for Basic Research; the Ministerio de Ciencia e

Innovación, and Programa Consolider-Ingenio 2010, Spain; the Slovak R&D Agency; the Academy of Finland; and the Australian Research Council (ARC).

---

[1] P. W. Higgs, Phys. Rev. Lett. **13**, 508 (1964).

[2] The TEVNPH Working Group (2010), arXiv:1007.4587 [hep-ex].

[3] J. Alcaraz et al. (ALEPH, DELPHI, L3, and OPAL collaborations and the LEP Electroweak Working Group) (2008), hep-ex/arXiv:0811.4682.

[4] A. Djouadi, J. Kalinowski, and M. Spira, Comput. Phys. Commun. **108**, 56 (1998).

[5] T. Aaltonen et al. (CDF Collaboration), Phys. Rev. D. **80**, 012002 (2009).

[6] V. A. et al. (The D0 collaboration), Phys. Rev. Lett. **102**, 051803 (2009), arXiv:0808.1970.

[7] D. Acosta et al. (CDF collaboration), Phys. Rev. D **71**, 052003 (2005).

[8] T. A. et al (The CDF Collaboration), Phys. Rev. Lett. **103**, 101802 (2009).

[9] D. Acosta et al. (CDF collaboration), Phys. Rev. D **71**, 032001 (2005).

[10] L. Balka et al., Nucl. Instrum. Methods A **267**, 272 (1988).

[11] S. Bertolucci et al., Nucl. Instrum. Methods A **267**, 301 (1988).

[12] M. G. Albrow et al., Nucl. Instrum. Methods A **480**, 524 (2002).

[13] F. Abe et al. (CDF collaboration), Phys. Rev. D **45**, 1448 (1992).

[14] A. Bhatti et al., Nucl. Instrum. Methods A **566**, 375 (2006).

[15] G. Ascoli et al., Nucl. Instrum. Methods A **268**, 33 (1988).

[16] T. Dorigo (CDF collaboration), Nucl. Instrum. Methods A **461**, 560 (2001).

[17] E. J. Thomson et al., IEEE Trans. Nucl. Sci. **49**, 1063 (2002).

[18] T. Aaltonen et al. (CDF Collaboration), Phys. Rev. Lett. **100, 211801** (2008).

[19] D. Acosta et al. (CDF collaboration), Phys. Rev. Lett. **94**, 091803 (2005).

[20] T. Aaltonen et al. (CDF Collaboration), Phys. Rev. D **79**, 112007 (2009).

[21] A. Abulencia et al. (CDF collaboration), Phys. Rev. Lett. **97**, 082004 (2006).

[22] A. Abulencia et al. (CDF collaboration), Phys. Rev. D **74**, 072006 (2006).

[23] T. A. et al (The CDF Collaboration), Phys. Rev. D **82**, 112005 (2010), arXiv:1004.1181.

[24] T. Aaltonen et al. (CDF Collaboration), Phys. Rev. Lett. **101**, 252001 (2008).

[25] T. Aaltonen et al. (CDF collaboration), Phys. Rev. Lett. **100**, 041801 (2008).

[26] J. Campbell and R. K. Ellis, Phys. Rev. D **65**, 113007 (2002).

[27] M. Cacciari, S. Frixione, M. L. Mangano, P. Nason, and G. Ridolfi, J. High Energy Phys. **04**, 068 (2004).

[28] B. W. Harris, E. Laenen, L. Phaf, Z. Sullivan, and S. Weinzierl, Phys. Rev. D **66**, 054024 (2002).

[29] M. L. Mangano, M. Moretti, F. Piccinini, R. Pittau, and A. D. Polosa, J. High Energy Phys. **07**, 001 (2003).

[30] G. Corcella et al., CERN-TH **2001-369** (2001).

[31] T. Sjöstrand et al., Comput. Phys. Commun. **135**, 238 (2001).

[32] A. Abulencia et al. (CDF collaboration), Phys. Rev. D **73**, 032003 (2006).

[33] J. Pumplin et al., J. High Energy Phys. **07**, 012 (2002).

[34] T. Junk, Nucl. Instrum. Methods A **434**, 435 (1999).